

Microstructure and Pressure Driven Electrodeposition Stability in Solid-State Batteries

Ankit Verma¹, Hiroki Kawakami², Hiroyuki Wada², Anna Hirowatari², Nobuhisa Ikeda², Yoshifumi Mizuno², Toshikazu Kotaka², Koichiro Aotani², Yuichiro Tabuchi², and Partha P. Mukherjee^{1z}

¹School of Mechanical Engineering, Purdue University, West Lafayette, IN, USA

²Nissan Research Center, Nissan Motor Co., Ltd., Natsushima, Yokosuka, Kanagawa 237-8523, Japan

^zCorresponding author: pmukherjee@purdue.edu

Abstract

Interfacial deposition stability at the lithium metal-solid electrolyte interface in all solid-state batteries (ASSB) is governed by the stress-transport-electrochemistry coupling in conjunction with the polycrystalline/amorphous solid electrolyte architecture. In this work, we delineate the optimal solid electrolyte microstructure comprising of grains, grain boundary and voids possessing desirable ionic conductivity and elastic modulus for superior transport and strength. An analytical formalism is provided to discern the impact of external “stack” pressure induced mechanical stress on electrodeposition stability; stress magnitude obtained are in the megapascal range considerably diminishing the stress-kinetics effects. For experimental stack pressures ranging up to 10 MPa, the impact of stress on reaction kinetics is negligibly small and electrolyte transport overpotentials dictate electrodeposition stability. We detail the deposition stability phase map as a function of solid electrolyte to Li metal shear modulus and molar volume ratios under varying operating conditions including external pressure, surface roughness, applied current density and ambient temperature. High current density operation with stable deposition can be ensured with ample external pressure, high temperature and low surface roughness operation for low shear modulus ratio of the solid electrolyte to Li metal.

Keywords: Solid electrolyte, Li metal, polycrystalline, grain boundary, void, external pressure

Introduction

Lithium-ion batteries (LIBs) have become pervasive in small scale electronics and are gearing towards high energy, power applications like electric vehicles and grid energy storage¹. Commercial LIBs with graphite anode, transition metal oxide cathodes and liquid electrolyte operate through shuttling of Li⁺ ions between the intercalation hosts. Graphite (specific capacity ~ 372 mAh/g)² and metal oxide (specific capacity ~ 200 mAh/g)³ host structure lowers the cell gravimetric/volumetric specific capacity, consequently, large battery packs comprising of several unit cells are required for high energy/power applications. The development of next generation lithium-ion batteries with enhanced energy and power density is predicated on utilization of pristine lithium metal anodes, which exhibit low reduction potential (-3.04 V) and high specific capacity (3870 mAh/g)⁴. In this configuration, entire anode mass contributes to the cell capacity precluding the inactive weight associated with the carbonaceous host. However, several problems plague the usage of Li metal anodes in LIBs. Immense volumetric fluctuations during the plating-stripping process coupled with heterogeneous metal nucleation and growth leads to solid electrolyte interphase (SEI) breakdown-reformation loop and dead lithium accumulation during each cycle contributing to rapid capacity fade.⁵⁻⁶ Uninhibited dendritic growth at the anode during charging poses a serious safety issue; dendritic growth through the porous separator in liquid electrolytes can reach the cathode causing internal short circuit-based failure of the metal battery system.⁷

Dendrite growth suppression using all solid-state batteries (ASSBs) comprising of solid electrolytes (SEs) providing a rigid barrier against Li deposition has emerged as a promising growth control strategy.⁸⁻¹⁰ Solid electrolyte systems also offer improved safety, no leakage, non-flammability and a larger electrochemical window. During the past decade, several SEs with ionic conductivity similar to liquid electrolytes have been developed¹¹⁻¹⁵. However, there

are some bottlenecks afflicting the performance of solid-state batteries as well¹⁶. High interfacial resistance due to low chemical/mechanical wettability, unstable nature of the metal-SE interface resulting in chemical/electrochemical decomposition based interphase formation and imperfect contact are major hindrances that need to be overcome¹⁷⁻¹⁸. SE decomposition at the electrode/electrolyte interface leads to the formation of interphase layer while sluggish interfacial transport leads to the formation of Li-ion depletion zones¹⁹⁻²⁰. Imperfect contact between the metal-electrolyte interface leads to current focusing at junctions, reducing the interfacial charge transfer area considerably and result in large kinetic overpotentials²¹. Furthermore, stress evolution inside the SE resulting from heterogeneous deposition can surpass its material fracture strength, causing fracture, and impede the Li-ion transport in electrolyte appreciably.²² The cathode-solid electrolyte composite also suffers from dynamic stress and fracture during cycling arising from diffusion-induced stress and contact mechanics²³⁻²⁴.

Polymer²⁵⁻²⁸, garnet²⁹⁻³⁴ and sulfide³⁵⁻³⁷ electrolytes primarily comprise the array of SEs being investigated for applications in solid-state batteries to mitigate dendrite growth. Single-ion conductors with unity transference numbers (inorganic garnet, sulfide SEs) have attracted renewed interest recently³⁸. While sulfide electrolytes like LPS generally exhibit glassy/amorphous structure³⁹⁻⁴⁰, garnet oxide electrolytes like LLZO exhibit polycrystalline structure⁴¹⁻⁴². Polycrystalline structure of garnet electrolytes has been identified as the cause of unmitigated Li growth through the electrolyte beyond critical current densities (CCD) through preferential growth along the grain boundaries as observed in experiments⁴³. Transgranular growth of Li has also been proposed, although, propagation through grain boundaries form majority of experimental findings. Single crystal SEs have exhibited penetration by Li dendrite as well.^{33, 44} Experimentally, several strategies are being explored to ensure deposition stability with inorganic electrolytes including the use of electrochemically stable artificial interlayers

juxtaposed between the Li metal and SE (eliminates interphase formation through metal-SE decomposition)^{20, 45-50} and external mechanical “stack” pressure application (promotes interfacial contact reducing contact resistance)⁵¹⁻⁵³ on the metal-SE system.

Electrodeposition at solid-solid interfaces is affected by interfacial stresses as demonstrated by the seminal theoretical work of Monroe and Newman⁵⁴. Further analysis of Li-solid polymer electrolyte systems using linear elasticity theory and stress-kinetics coupling was pioneered by Monroe and Newman; it was demonstrated that a SE with shear modulus twice that of Li metal was capable of suppressing dendrite growth⁵⁵. This work was extended by Barai *et al.* incorporating ion transport through the SE and elastic-plastic deformation of lithium for solid polymer electrolyte⁵⁶. The above analysis has been recently extended to solid inorganic electrolytes to account for the varying partial molar volumes of Li in polymer electrolyte vs solid inorganic electrolyte⁵⁷⁻⁵⁸. A unifying theme of the above studies was the large interfacial stress magnitudes (gigapascals) impacting the deposition stability through ion flux redistribution towards/away from the metal protrusions. The impact of polycrystalline SE architecture on deposition stability and delineation of current focusing in the grain boundaries for nanometer-sized grains have been studied as well^{22, 59}. However, realistic SEs can be of the size of hundreds of microns with grain size lying in the micrometer range⁶⁰. Furthermore, experimental data suggests that even for sufficiently high shear modulus electrolytes, Li metal penetration through the SE is unavoidable⁴⁴. These findings necessitate detailed investigation of the mechanisms of growth and the correlation between the critical current density, transport–electrochemistry-mechanics complexations of the Li metal substrate and SE microstructure (grain boundaries, defects, pores, imperfect contact) under external pressure and varying thermal environments. There is a need for a coupled physics-based model to delineate stable operating regimes of the solid-state battery with inorganic SE under external pressure⁶¹⁻⁶⁴. There is now a concerted effort to understand the coupled effects of stress, surface defects,

interfacial resistance, plasticity on Li electrodeposition with a focus on continuum-level modeling studies⁶⁵⁻⁶⁸.

In this work, we use a combined experiment-modeling paradigm to elucidate the deposition stability of the metal-inorganic SE system cognizant of practical ASSB system physics. Firstly, the amorphous/polycrystalline microstructure of inorganic SEs comprising of grains, grain boundaries and voids is characterized to obtain the effective transport and mechanical parameters governing deposition dynamics. The effective property computations help in discerning the optimal microstructural configuration of the SE with superior transport and strength. Subsequently, we discern the impact of external pressure on the deposition characteristics. Stress in the metal-SE system under external pressure is directly correlated to the stack pressure magnitudes, lying primarily in the megapascal range. Consequently, the impact of stress-kinetics coupling on deposition stability is considerably reduced. Finally, we give the stability map for inorganic SE-Li metal system as a function of its mechanical and thermodynamic parameters (shear modulus ratio and molar volume ratio) for a wide range of operating conditions, namely, external pressure, applied current density, surface roughness and working temperature. They provide good qualitative match to experimental datasets for the amorphous and polycrystalline LPS SE system.

Methodology

Experimental Methods

Synthesis: Amorphous LPS electrolyte (a-LPS) = 75Li₂S-25P₂S₅, and the crystalline LPS electrolyte (c-LPS) = β -Li₃PS₄, were synthesized from Li₂S powder (>99.9 % purity, Mitsuwa Chemical) and P₂S₅ powder (>99 % purity, Sigma-Aldrich). The two powders were weighed (molar ratio of Li₂S/P₂S₅ = 75/25) and mixed in agate mortar with agate pestle. As for a-LPS electrolyte, the mixture was milled with planetary ball milling apparatus at 370 rpm for 40

hours. The pellet of a-LPS (thickness 700 μm) was obtained by putting milled mixture (100 mg) into Φ 10 mm (diameter) ceramic tube and then compressing at 360 MPa and heating at 190 °C for 1 hour. In the case of c-LPS, mixed powder was milled at 250 rpm for 40 hours. c-LPS electrolyte was obtained by firing the mixture at 300 °C for 16 hours and then pulverizing by ball milling at 50 rpm for 2.5 hours. c-LPS electrolyte was pelletized (thickness 700 μm) by putting c-LPS (100 mg) powder into Φ 10 mm ceramic tube and compressing at 380 MPa and ambient temperature for 1 minute. All the procedures were conducted in argon atmosphere.

Preparation of the Li-symmetrical cell: Lithium foils (Honjo Metal, Φ 5 mm, thickness 100 μm) were placed on both surfaces of obtained solid electrolyte pellet and then sandwiched between two stainless steel rods as a current collector. The pressure of 1.5 MPa (solid electrolyte a-LPS) and 1.5 MPa-7 MPa (solid electrolyte c-LPS), respectively, was applied to stainless steel/lithium/solid electrolyte/lithium/stainless steel layers. Obtained Li-symmetrical cell were put into a sealed container. The sealed container was full of argon gas and we could apply voltage or current to the cell inside. Li-symmetrical cell preparation was carried out in glove box filled with argon gas at ambient temperature.

Measurement of elastic property: The obtained pellets were used as samples to measure the Young's modulus. Young's moduli were measured in Ar-filled grove box by using nanoindentation (Hysitron, TI-980) with spherical indenter (tip radius: 100 μm) under a maximum load range of 50 mN and at the room temperature 23 °C. The measured Young's moduli for a-LPS and c-LPS are tabulated in Table 1.

Measurement of ionic conductivity: Prepared Li-symmetrical cell were used as samples for the measurement. The ionic conductivity was measured by the AC impedance analyzer (AMETEK, 1260A Impedance/gain-phase Analyzer) in the frequency range 1 Hz to 10 MHz in thermostatic chamber. The characterization experiments are run at multiple temperatures

ranging from 25°C to 100°C to obtain the activation energy for ionic conductivity. The measured ionic conductivities and the activation energy for a-LPS and c-LPS are summarised in Table 1.

Measurement of the exchange current density: Direct current approach is used to measure the exchange current density of through the best fit of the Butler-Volmer equation to the oxidation-reduction potential vs current density data (current density is varied from 0.1 to 10 mA/cm²). Li-symmetrical cell whose electrodes were Li-In alloy and electrolyte was Li₁₀GeP₂S₁₂ was used for measurement of the exchange current density. The activation energy for the exchange current density was obtained by measurement with two temperature, 25 °C and 60 °C. The value of the exchange current density and the activation energy are shown in Table 1.

Measurement of critical current density: Critical current density (CCD) was measured by direct current cycling (TOYO, TOSCAT-3100) in thermostatic chamber-and in the temperature range 60°C to 100°C. Capacity of charge and discharge per each applied current density step is 0.1 mAh/cm² and applied current density is stepwisely increased by 0.1 mA/cm² (0.1-1 mA/cm²) and by 1 mA/cm² (>1 mA/cm²), respectively. Current density which was applied in the step before sudden rise/drop in polarization voltage occurred was determined as CCD.

Computational Methods

The schematic of the model geometry used for our computations is shown in Figure 1. The SE domain (blue) lies on top of the Li metal domain (grey) with perfect conformal contact. The metal-electrolyte surface roughness is represented by a sinusoidal interfacial perturbation allowing for the computation of stresses using linear elastic perturbation theory⁶⁹⁻⁷². The metal-electrolyte system is reduced to a two-dimensional geometry with isotropic mechanical and transport properties. The applied external pressure generates mechanical stresses inside our

system, with differing magnitudes at the peaks and the valleys. Lithium-ion flux from the SE corresponding to the applied current density, i_{app} , redistributes at the Li protrusions (peaks) and the Li depressions (valleys) of the interface in accordance with transport through the SE and interfacial stresses and the subsequent deposition stability can be characterized through the magnitude of the peak to valley current density ratio, i_{peak} / i_{valley} or i_p / i_v . This criterion is widely used in literature to understand deposition characteristics^{22, 55-57}. A magnitude of $i_{peak} / i_{valley} > 1$ corresponds to preferential growth of the peaks as opposed to the valley resulting in an enhancement of surface roughness leading to unstable deposition. Conversely, a magnitude of $i_{peak} / i_{valley} \leq 1$ results in eventual flattening of the interfacial perturbation leading to stable deposition. The architecture of the SE, polycrystalline or amorphous, determine the effective transport and elastic properties, having an impact on the deposition stability. A polycrystalline architecture comprises of grains, grain boundaries and voids with different values of ionic conductivity and elastic constant attributed to each phase while an amorphous architecture can be characterized through the presence of grains and voids.

The analysis involves the following steps:

- Virtual generation of *polycrystalline* and *amorphous* SE microstructure for computation of effective transport and elastic constants.
- Effective property computation on the voxelated microstructure mesh with intrinsic properties attributed to each of the grain, grain boundary and void phase.
- Electrodeposition stability analysis on the SE-Li metal system cognizant of the external pressure-based stress considerations, stress-kinetics coupling at the metal-electrolyte interface and ionic transport through the SE

Virtual Microstructure Generation and Effective Property Calculations

Figure 2 show the representative microstructures for polycrystalline and amorphous SE system. A polycrystalline structure comprises of grains (G), grain boundaries (GB) and voids (V) while the amorphous structure consists of grains and voids⁷³⁻⁷⁴. Experimentally, SEM images of the electrolyte can be used to characterize the grain and void size while the relative density values can be used to compute the porosity of the electrolyte. The virtual microstructures are generated using the software suite DREAM.3D which allows for the screening of a wide range of grain size, void size, and void fractions⁷⁵. Figure 2(a-i) exhibits the three-dimensional polycrystalline SE without voids and a grain size of 10 μm , while Figure 2(a-ii) displays a polycrystalline SE containing voids with a larger grain size of 20 μm . The voids are of size 4 μm with the pore volume fraction 25%. Figure 2(b) shows the front view of the polycrystalline SE with varying grain size, void size and porosity. The grains are shown in yellow, grain boundaries in red and voids in blue. As we move from the left to right, the grain size - void size - porosity varies from (b-i) 5 μm – 4 μm – 5%, (b-ii) 10 μm – 4 μm – 5%, (b-iii) 5 μm – 10 μm – 5% to (d) 5 μm – 4 μm – 20%. As the grain size increases, the grain boundary density decreases. As the void size increases, the number of voids for the same void volume decreases. Figure 2(c) shows the representative amorphous SE microstructure with varying void size and porosity. As we move from left to right, the void size – porosity varies from (c-i) 4 μm - 5%, (c-ii) 10 μm – 5% to (c-iii) 4 μm – 20%. There are no grain boundaries in the amorphous SE. It is to be noted that realistically, voids usually reside within the grain boundaries, or triple junction points. However, there exist some cases where voids are observed to occur inside grains as well. To account for that, the void distribution during microstructure generation in DREAM.3D has been taken to be 50% at the grain boundaries and triple junctions and 50% inside the grain.

Effective electrolyte properties are obtained by doing Direct Numerical Simulation (DNS) calculations on the reconstructed virtual SE microstructure. The effective electrolyte

ionic conductivity and elastic modulus depends on arrangement of the grains, grain boundaries and voids and their intrinsic values. The DNS calculations involve the solution of Laplace equation on three-dimensional electrode microstructure grid with Dirichlet boundary conditions along the transport/stress direction and periodic boundary conditions on the other four faces. We assign a finite thickness to the grain boundary for the effective property computations on a voxelated mesh, with the grain boundary thickness ranging from 10 nm to 100 nm⁷⁶. The grain boundary thickness of 10 nm represents the closest analogue to the realistic structure. In-house codes are used to characterize the effective ionic conductivity and elastic constants. The representative elementary volume is ensured to be approximately 10 times the biggest feature size to ensure grid independence of the properties, and the voxel resolution is kept equal to the smallest feature size, namely, the grain boundary thickness. High performance computing was utilized to enable effective property computations for large grid sizes.

The effective ionic conductivity can be calculated by solving the Laplace's equation for electrolyte potential $\nabla \cdot (\kappa_{SE,ref} \nabla \phi) = 0$ with the individual phases assigned their intrinsic reference ionic conductivities.

$$\kappa_{SE,ref}(\vec{x}) = \begin{cases} \kappa_G & \text{if } \vec{x} \in G \\ 0.01\kappa_G & \text{if } \vec{x} \in GB \\ 0 & \text{if } \vec{x} \in V \end{cases} \quad (1)$$

$$\kappa_{SE,ref,x}^{eff} = \frac{L}{A(\phi_{right} - \phi_{left})} \int_{\Omega_x} \kappa_{SE} \frac{\partial \phi}{\partial x} dy dz \quad (2)$$

Here, the grain boundary conductivity is assigned an intrinsic value of 0.01 times the conductivity of the grain in accordance with density functional theory computations of grain boundary transport⁷⁷⁻⁷⁸. They show that grain boundary transport of Li⁺ is sluggish as compared to the Li⁺ intragrain transport. The effective conductivities in the y and z-directions are

computed in the usual fashion and an arithmetic mean is used to calculate the effective ionic conductivity of the full 3D structure, $\kappa_{SE,ref}^{eff} = (\kappa_{SE,ref,x}^{eff} + \kappa_{SE,ref,y}^{eff} + \kappa_{SE,ref,z}^{eff}) / 3.0$. It is to be noted here that there is recent work which proposes that grain boundary ionic conductivity can be larger than the bulk conductivity⁷⁹ and the solid electrolyte can have intrinsic electronic conductivity with high electronic conductivity proposed as the origin of lithium dendrite formation within solid electrolytes⁸⁰. For the sake of simplicity of analysis, we have neglected the aforementioned physical phenomena. These assumptions becomes more sensible for large grain size (>25 μm) wherein the inherent grain boundary volume inside the solid electrolyte architecture with grain boundary thickness 10 nm is inherently low resulting in marginal effect of the grain boundaries on effective property computations.

Similarly, the effective elastic modulus can be calculated by solving the Laplace's equation for displacement $\nabla \cdot (E_{SE} \nabla u) = 0$ with the individual phases assigned their intrinsic elastic modulus.

$$E_{SE}(\vec{x}) = \begin{cases} E_G & \text{if } \vec{x} \in G \\ 0.5E_G & \text{if } \vec{x} \in GB \\ 0 & \text{if } \vec{x} \in V \end{cases} \quad (3)$$

$$E_{x,eff} = \frac{L}{A(u_{right} - u_{left})} \int_{\Omega_x} E_{SE} \frac{\partial u}{\partial x} dy dz \quad (4)$$

Here, the grain boundary elastic modulus is assigned an intrinsic value of 0.5 times the elastic modulus of the grain in accordance with density functional theory computations by Seungho *et al*⁸¹. This complies with the grain boundary softening mechanism through which the dendrites can penetrate the SE. It is to be noted that our stiffness computations have an inherent inaccuracy in the sense that the displacement field being solved for is not a scalar quantity. For force that is applied along the x -direction, there will be displacement or stress generation along

the y and z -directions. However, as a first approximation the resulting effective Young's modulus magnitudes obtained can be taken to be similar to the solution of the exact displacement partial differential equation given by Eq. (7) in the Supplementary Information.

Electrochemistry-Transport-Stress Model

Since, the garnet and sulfide electrolytes are single-ion conductors with immobile anionic species, Li^+ transport occurs only through migration and concentration gradients cannot develop inside the SE due to violation of electroneutrality⁸². Hence, the corresponding governing differential equation and boundary conditions for ion transport through the electrolyte domain take the following form.

$$\vec{\nabla} \cdot (\kappa_{SE}^{eff} \vec{\nabla} \phi_e) = 0 \quad (5)$$

$$\begin{aligned} -\kappa_{SE}^{eff} \vec{\nabla} \phi_e &= i_{app} && \text{at solid electrolyte - top interface} \\ -\kappa_{SE}^{eff} \vec{\nabla} \phi_e &= i_{BV} && \text{at solid electrolyte - Li metal interface} \\ -\kappa_{SE}^{eff} \vec{\nabla} \phi_e &= 0 && \text{at left and right boundaries} \end{aligned} \quad (6)$$

$$\kappa_{SE}^{eff} = \kappa_{SE,ref}^{eff} \left[\frac{-E_{a,\kappa}}{R} \left(\frac{1}{T} - \frac{1}{T_{ref}} \right) \right] \quad (7)$$

Here, ϕ_e is electrolyte phase potential, i_{app} is the applied current density entering the SE domain. Ionic conductivity of the SE shows an Arrhenius dependence⁸³ on the operating temperature T with activation energy $E_{a,\kappa}$ and reference values are given at $T_{ref} = 25^\circ\text{C}$. i_{BV} is the electrochemical current density at the Li metal- electrolyte interface given by the modified Butler-Volmer kinetics,

$$i_{BV} = i_0 \exp \left[\left(1 - \alpha_a \right) \frac{\Delta \mu_{e^-}}{RT} \right] \left[\exp \left(\frac{\alpha_a F}{RT} \eta \right) - \exp \left(- \frac{\alpha_c F}{RT} \eta \right) \right] \quad (8)$$

$$i_0 = i_{0,ref} \exp \left[-\frac{E_{a,i0}}{R} \left(\frac{1}{T} - \frac{1}{T_{ref}} \right) \right] \quad (9)$$

Here, i_0 is the exchange current density for the electrochemical reaction at the metal-electrolyte interface at absolute temperature T . It exhibits an Arrhenius dependence on the operating temperature with activation energy $E_{a,i0}$ and reference values are given at $T_{ref} = 25^\circ\text{C}$.

$\alpha_a, \alpha_c = 0.5$ are the anodic and cathodic charge transfer coefficients, F is Faraday's constant and R is the universal gas constant. Surface overpotential for the plating reaction is defined as,

$\eta = \phi_s - \phi_e - U_{Li} + (\Delta\mu_{e^-} / F)$, where ϕ_s is the solid phase potential and U_{Li} is the open circuit potential of Li. Given that the open circuit potential of Li vs Li is equal to zero, this overpotential reduces to $\eta = \phi_s - \phi_e + (\Delta\mu_{e^-} / F)$. Furthermore, the Li metal electronic conductivity is sufficiently high ($\sim 10^7$ S/m) allowing the solid phase potential to be set to zero all throughout the Li metal domain. The corresponding surface overpotential for the plating reaction now takes the form $\eta = -\phi_e + (\Delta\mu_{e^-} / F)$.

The stress-kinetics coupling is exemplified by the $\Delta\mu_{e^-}$ term which indicates the electrochemical potential change due to mechanical stress⁵⁵⁻⁵⁶. The electrochemical potential change due to strain energy can be expressed in terms of the mechanical stress, $\vec{\sigma}$, and partial molar volumes of the lithium metal, \bar{V}_{Li} , and SE, \bar{V}_{SE} , as

$$\mu_{e^-} = -\frac{1}{2}(\bar{V}_{Li} + \bar{V}_{SE})(\gamma\hat{\kappa} + \vec{n} \cdot [\vec{n} \cdot (\vec{\tau}_{Li}^d - \vec{\tau}_{SE}^d)]) + \frac{1}{2}(\bar{V}_{Li} - \bar{V}_{SE})(p_{Li} + p_{SE}) \quad (10)$$

Here, γ is the surface energy, $\hat{\kappa}$ is the surface curvature of the Li metal-SE interface, \vec{n} is the unit normal vector at the lithium-SE interface directed into the SE, $\vec{\tau}_{Li}^d, \vec{\tau}_{SE}^d$ are the interfacial deviatoric stress tensors in the metallic Li and SE phase respectively, and p_{Li}, p_{SE} are the

interfacial hydrostatic stress in the lithium and SE domain respectively. It is to be noted that compressive hydrostatic stress is assumed to be positive here, while the deviatoric stress tensors follow the usual sign convention, i.e., tensile stresses are positive and compressive stresses are negative. Surface energy contributions to the electrochemical potential change, $\Delta\mu_e^-$, have been shown to be negligible in literature as compared to the stress^{55, 61}. The impact of surface energy on electrochemical potential change depends on the surface curvature⁸⁴. It is evident that a computation of the electrochemical potential change term requires computation of mechanical stress magnitudes throughout the system.

The analysis of stresses generated due to external pressure on the SE-Li metal domain is carried out assuming quasistatic mechanical equilibrium since pressure waves travel at the speed of sound allowing for instantaneous equilibration. Correspondingly, the governing differential equation for mechanical stress take the following form

$$\nabla \cdot \vec{\sigma} = 0 \quad (11)$$

In accordance with the linear elastic perturbation theory analysis, elastic mechanics is assumed for both the Li metal and the SE:

$$\vec{\sigma} = -\frac{2\nu G}{1-2\nu} \text{tr}(\vec{\varepsilon}) - 2G\vec{\varepsilon} \quad (12)$$

The top and bottom of the SE and Li metal domain are subjected to the constant external pressure boundary condition, $\vec{\sigma}\vec{n} = P_{ext}\vec{n}$, with the interfacial perturbation giving the displacement boundary condition at the interface, $v = A \cos(kx)$, alongside continuity of stress vector across the interface from force balance. The solution to the mechanical problem is computed by finding the Airy stress function which satisfies the biharmonic equation, $\Delta^4 \varphi = 0$. The stress components can be calculated from the relations

$$\sigma_{xx} = \frac{\partial^2 \varphi}{\partial y^2}, \quad \sigma_{yy} = \frac{\partial^2 \varphi}{\partial x^2}, \quad \sigma_{xy} = -\frac{\partial^2 \varphi}{\partial x \partial y} \quad (13)$$

The corresponding solution to the Airy stress functions takes the form:

$$\begin{aligned} \varphi_{SE} &= -\frac{|P_{ext}|}{2} \left(x^2 + \nu_{SE} y^2 \right) + \frac{-|P_{ext}| A \cos(kx) \exp(-ky) (\alpha_{SE} y + \beta)}{k (G_{Li} \tilde{\kappa}_{SE} + G_{SE}) (G_{SE} \tilde{\kappa}_{Li} + G_{Li})} \\ \varphi_{Li} &= -\frac{|P_{ext}|}{2} \left(x^2 + \nu_{Li} y^2 \right) + \frac{|P_{ext}| A \cos(kx) \exp(ky) (\alpha_{Li} y - \beta)}{k (G_{Li} \tilde{\kappa}_{SE} + G_{SE}) (G_{SE} \tilde{\kappa}_{Li} + G_{Li})} \end{aligned} \quad (14)$$

Here, the material specific constants are defined as

$$\begin{aligned} \tilde{\kappa}_{SE} &= 3 - 4\nu_{SE}, \quad \tilde{\kappa}_{Li} = 3 - 4\nu_{Li} \\ \alpha_{SE} &= k (1 - \nu_{SE}) (G_{Li} - G_{SE}) (G_{SE} \tilde{\kappa}_{Li} + G_{Li}) \\ \alpha_{Li} &= k (1 - \nu_{Li}) (G_{SE} - G_{Li}) (G_{Li} \tilde{\kappa}_{SE} + G_{SE}) \\ \beta &= 2G_{SE}^2 \frac{1 - \nu_{Li}}{1 + \nu_{Li}} - 2G_{Li}^2 \frac{1 - \nu_{SE}}{1 + \nu_{SE}} + 4G_{SE} G_{Li} \frac{\nu_{SE} - \nu_{Li}}{(1 + \nu_{Li})(1 + \nu_{SE})} \end{aligned} \quad (15)$$

From the Airy stress functions, the stress components can be calculated using double differentiations. For the solid electrolyte, the stress components are:

$$\sigma_{xx,SE} = -|P_{ext}| \nu_{SE} - \frac{|P_{ext}| A \cos(kx)}{k (G_{Li} \tilde{\kappa}_{SE} + G_{SE}) (G_{SE} \tilde{\kappa}_{Li} + G_{Li})} \left[k^2 \exp(-ky) (\alpha_{SE} y + \beta) - 2\alpha_{SE} k \exp(-ky) \right] \quad (16)$$

$$\sigma_{yy,SE} = -|P_{ext}| + \frac{|P_{ext}| Ak^2 \cos(kx) \exp(-ky) (\alpha_{SE} y + \beta)}{k (G_{Li} \tilde{\kappa}_{SE} + G_{SE}) (G_{SE} \tilde{\kappa}_{Li} + G_{Li})} \quad (17)$$

$$\sigma_{xy,SE} = -\frac{|P_{ext}| Ak \sin(kx)}{k (G_{Li} \tilde{\kappa}_{SE} + G_{SE}) (G_{SE} \tilde{\kappa}_{Li} + G_{Li})} \left[-k \exp(-ky) (\alpha_{SE} y + \beta) + \alpha_{SE} \exp(-ky) \right] \quad (18)$$

$$\sigma_{zz,SE} = \nu_{SE} (\sigma_{xx,SE} + \sigma_{yy,SE}), \quad \sigma_{yz,SE} = \sigma_{xz,SE} = 0 \quad (19)$$

For Li metal, the corresponding stress components are:

$$\sigma_{xx,Li} = -|P_{ext}|v_{Li} + \frac{|P_{ext}|A\cos(kx)}{k(G_{Li}\tilde{\kappa}_{SE} + G_{SE})(G_{SE}\tilde{\kappa}_{Li} + G_{Li})} [k^2 \exp(ky)(\alpha_{Li}y - \beta) + 2\alpha_{Li}k \exp(ky)] \quad (20)$$

$$\sigma_{yy,Li} = -|P_{ext}| - \frac{|P_{ext}|Ak^2 \cos(kx) \exp(ky)(\alpha_{Li}y - \beta)}{k(G_{Li}\tilde{\kappa}_{SE} + G_{SE})(G_{SE}\tilde{\kappa}_{Li} + G_{Li})} \quad (21)$$

$$\sigma_{xy,Li} = \frac{|P_{ext}|Ak \sin(kx)}{k(G_{Li}\tilde{\kappa}_{SE} + G_{SE})(G_{SE}\tilde{\kappa}_{Li} + G_{Li})} [k \exp(ky)(\alpha_{Li}y - \beta) + \alpha_{Li} \exp(ky)] \quad (22)$$

$$\sigma_{zz,Li} = v_{SE} (\sigma_{xx,Li} + \sigma_{yy,Li}), \quad \sigma_{yz,Li} = \sigma_{xz,Li} = 0 \quad (23)$$

For the plane strain constant pressure case, the hydrostatic and deviatoric stress tensors take the form:

$$\vec{p} = \begin{bmatrix} (\sigma_{xx} + \sigma_{yy} + \sigma_{zz})/3.0 & 0 & 0 \\ 0 & (\sigma_{xx} + \sigma_{yy} + \sigma_{zz})/3.0 & 0 \\ 0 & 0 & (\sigma_{xx} + \sigma_{yy} + \sigma_{zz})/3.0 \end{bmatrix} \quad (24)$$

$$\vec{\tau}^d = \begin{bmatrix} \frac{2}{3}\sigma_{xx} - \frac{1}{3}(\sigma_{yy} + \sigma_{zz}) & \sigma_{xy} & 0 \\ \sigma_{xy} & \frac{2}{3}\sigma_{yy} - \frac{1}{3}(\sigma_{xx} + \sigma_{zz}) & 0 \\ 0 & 0 & \frac{2}{3}\sigma_{zz} - \frac{1}{3}(\sigma_{xx} + \sigma_{yy}) \end{bmatrix} \quad (25)$$

Here I is the identity tensor. Please note here that compressive stress is taken to be positive in computation of the electrochemical potential change. The computation of the electrochemical potential change due to stress can subsequently be carried using Eq. (10) once

the normal vector to the interface, \vec{n} , is computed. We see that the deviatoric component of electrochemical stress change involves the dot product of a second order tensor, $\vec{\tau}^d$, with the normal vector which is a first order tensor (vector) with no z-component for the two-dimensional perturbation. For the ease of understanding of the reader, we give the form of how such a product is calculated

$$\vec{n} = n_1 \hat{i} + n_2 \hat{j} + 0 \hat{k}, \quad \vec{\tau}^d = \begin{bmatrix} \tau_{11} & \tau_{12} & 0 \\ \tau_{21} & \tau_{22} & 0 \\ 0 & 0 & \tau_{33} \end{bmatrix}$$

$$\begin{aligned} \vec{n} \cdot \vec{\tau}^d &= (n_1 \tau_{11} + n_2 \tau_{21} + 0 \cdot \tau_{31}) \hat{i} + (n_1 \tau_{12} + n_2 \tau_{22} + 0 \cdot 0) \hat{j} + (n_1 \cdot 0 + n_2 \cdot 0 + 0 \cdot \tau_{33}) \hat{k} \quad (26) \\ &= (n_1 \tau_{11} + n_2 \tau_{21}) \hat{i} + (n_1 \tau_{12} + n_2 \tau_{22}) \hat{j} + 0 \hat{k} \end{aligned}$$

Subsequently, the deviatoric component of the electrochemical potential change due to strain energy will take the form

$$\vec{n} \cdot \vec{n} \cdot \vec{\tau}^d = n_1 (n_1 \tau_{11} + n_2 \tau_{21}) + n_2 (n_1 \tau_{12} + n_2 \tau_{22}) \quad (27)$$

For a detailed derivation of the stress equations and the constitutive constants, the reader is referred to the Angheluta *et al*⁸⁵ and the Supplementary Information (SI). An interesting observation is the exponential decay of the perturbation effect in the form of $\exp(|ky|)$ at positions away from the interface. The plane strain configuration has been used as it closely mimics the stress state in the Li metal-solid electrolyte assembly.

Results and Discussion

Electrolyte Microstructure Optimization

Figure 3 shows the contour maps of effective transport (ionic conductivity) and mechanical (elastic modulus) properties for the polycrystalline SE system as a function of the grain size, void size and porosity. Figures 3(a) and (b) give the effective ionic conductivity and Young's modulus for the grain boundary thickness $\delta = 10 \text{ nm}$. As the porosity increases for a

fixed grain size, it is evident that the effective ionic conductivity decreases rapidly (see figure 3(a)). For a porosity of 25%, the effective conductivity is reduced to 65% of the nominal value. The presence of voids hinders ion transport through the SE considerably and the Li^+ ions must move along tortuous pathways around the voids. Conversely, the impact of grain size on effective ionic conductivity is significantly less as compared to porosity; for a fixed porosity, effective conductivity increases marginally as the grain size is increased from 1 micron to 25 microns and beyond 25 microns it remains approximately constant. This is because for grain boundary thickness $\delta = 10 \text{ nm}$, the corresponding grain boundary volume is less than 3% even for the smallest grain size of $1 \mu\text{m}$. The grain boundary impedes ion transport as its ionic conductivity is 1% of the grain conductivity. However, its impact is seen only at very low grain sizes where the grain boundary density is the highest. As the grain size increases, the grain boundary density decreases with grain boundary volume $<0.12\%$ for grain size $25 \mu\text{m}$ and above. Consequently, grain size of $25 \mu\text{m}$ and above possess enough ion conduction pathways to increase its ionic conductivity to the nominal value. We see a similar trend with porosity and grain size for the effective Young's modulus in Figure 3(b). The impact of porosity on Young's modulus is synonymous to its effect on ionic conductivity. As the porosity increases, the SE becomes softer due to the presence of voids which do not provide any stiffness. The grain size effect on Young's modulus is significantly more negligible than on ionic conductivity. This is because grain boundary stiffness is approximately 50% of the grain stiffness while the corresponding ionic conductivity ratio is 0.01. Consequently, SE microstructure should be optimized for the effective ionic conductivity; a SE microstructure with good transport characteristics will automatically have adequate stiffness. The SE should be packed tightly to avoid void formation; a porosity less than 5% is desirable.

Figures 3(c) and (d) exhibit the effective ionic conductivity and Young's modulus for the SE system when the grain boundary thickness is increased to 100 nm. Now we see a more

discernible trend of ionic conductivity with grain size. As the grain size increases from 1 μm to 50 μm , there is a significant increase in ionic conductivity. Grain boundary volume for 1 μm grain size is approximately 23% which reduces to nearly 0.1% when the grain size is 50 μm . The polycrystalline SE has favorable transport and mechanical properties when the grain boundary density is minuscule. The contour plot of Young's modulus exhibits a similar trend. As porosity increases, stiffness decreases rapidly; as the grain size increases beyond 50 μm , the nominal Young's modulus is achieved.

Figures 3(e) and (f) depict the void size impact on effective properties along with porosity for a grain boundary thickness of 10 nm. No discernible impact of void size is seen; there are minor variations in the effective ionic conductivity and stiffness with void size. Heuristically, void sizes should be kept as small as possible; the presence of large voids may lead to highly tortuous pathways and if a void is present close to the electrode-electrolyte interface, it may render that portion of the interface electrochemically inactive. Pore connectivity has an impact on the critical current density as well; SE with interconnected pores short circuits earlier as opposed to one with less connected pores.⁸⁶ For an optimal polycrystalline SE microstructure, the design criteria is outlined here: grain size $\geq 25 \mu\text{m}$, void size $\leq 1 \mu\text{m}$ and porosity $< 5\%$. If the grain boundary thickness increases to 100 nm, the grain size should be increased to 50 μm and above. The above criteria are valid for amorphous SEs as well.

Impact of External Pressure

Figure 4 shows the stress computations in the Li metal-SE domain for varying boundary conditions and interfacial surface roughness. Here, surface roughness, S_R , is related to the perturbation amplitude, A , as $S_R = 2A$. The Li metal and SE domain sizes are 100 $\mu\text{m} \times 100 \mu\text{m}$ each; with a surface roughness of 1 μm and wavenumber, $k = 6.2832 \times 10^4$ ensuring that $Ak \ll 1$. In particular, figure 4(a) displays the stress contours for the normal, (i)

σ_{xx} , (ii) σ_{yy} , and shear stress components of the stress tensor, (iii) σ_{xy} , for the zero-displacement boundary condition at the top and bottom surfaces of SE and Li metal respectively. This configuration is taken from the Monroe and Newman⁵⁵ along with the stress solutions reported therein. The stress solutions are also reported in the Supplementary Information. The Li metal peaks lie at the $x = 0 \mu\text{m}$ and $x = 100 \mu\text{m}$ while the center region $x = 50 \mu\text{m}$ corresponds to the Li metal valley. The interface perturbation has been shown using a white line on the σ_{yy} contour plot. It is interesting to note that the stress magnitudes for this configuration lies in the gigapascal range. Correspondingly, since the interfacial stress magnitudes are high, its impact on the chemical potential change due to stress, $\Delta\mu_{e^-}$ is significant. For the SE to Li shear modulus ratio, G_{SE}/G_{Li} , ranging from 0.0 to 3.0 and molar volume ratio, $V_{SE}/V_{Li} = 12.88$, the chemical potential change magnitudes is of the order of 100 kJ/mol for a surface roughness of 8 nm with $Ak = 0.4$.⁵⁵ The contributions of chemical potential change to the current density is further amplified because of the exponential nature of the corresponding term in the current density modified Butler-Volmer expression, $\exp\left[(1-\alpha_a)\frac{\Delta\mu_{e^-}}{RT}\right]$. Correspondingly, we can see the amplified stress effects on current density distribution resulting in redistribution of current flux away from the peaks for a shear modulus of the solid electrolyte twice that of the Li metal.

In contrast, figures 4(b) and 4(c) display the stress contours in the Li metal-SE domain under the external pressure boundary condition. The top and bottom surfaces of the SE and Li metal are subjected to 10 MPa pressure respectively. Figure 4(b) displays the stress contours for the normal, (i) σ_{xx} , (ii) σ_{yy} , and shear stress components of the stress tensor, (iii) σ_{xy} , for the 10 MPa external pressure and surface roughness of 1 nm. The minuscule surface roughness is chosen to check the fidelity of the stress solve; it nearly approximates a flat interface. This

is further exemplified by the nearly flat white line in the σ_{yy} contour plot. For a flat interface, the y -direction normal stress should converge to the external pressure magnitude, which is exemplified in Figure 4(b-ii). The σ_{yy} values lie close to -10 MPa throughout the solid electrolyte and Li metal, implying the compressive nature of the stress. At the far-field away from the interface, σ_{yy} , takes the external pressure value, matching the specified boundary conditions. Furthermore, a flat interface under normal loading should be devoid of shear stresses. The stress contours for σ_{xy} show this behavior with shear stress magnitudes of the order of 10^{-4} MPa. The x -direction normal stress shows a stress discontinuity at the interface which is to be expected.

Figure 4(c) displays the stress contours for the normal, (i) σ_{xx} , (ii) σ_{yy} , and shear stress components of the stress tensor, (iii) σ_{xy} , for the 10 MPa external pressure and surface roughness of 1 μm . An increase in the perturbation amplitude changes the stress contours slightly, although, the y -direction normal stress still lies close to 10 MPa. An important point to note is that with the external pressure boundary condition, the stresses inside the system lie in the megapascal range close to the external pressure magnitude. This is nearly three orders of magnitude smaller as compared to the zero-displacement boundary condition. The corresponding chemical potential change is of the order of J/mol instead of kJ/mol. Subsequently, stress impact on reaction kinetics gets reduced considerably with the $\exp\left[\left(1-\alpha_a\right)\frac{\Delta\mu_{e^-}}{RT}\right]$ term taking values very close to 1. This implies that the impact of interfacial stress on heterogeneous current density distribution at the Li-SE interface is minuscule, and the major contributions to the deposition instability stem from the ion transport limitations. This observation is also seen in Tu *et al.*⁸⁷ Furthermore, the surface overpotential for the plating reaction given by $\eta = -\phi_e + \left(\Delta\mu_{e^-} / F\right)$ can be further approximated to $\eta = -\phi_e$

since $\Delta\mu_{e^-} / F$ magnitudes are of the order of 10^{-4} V. The σ_{zz} stress contours are shown in Figure S1 in the Supplementary Information. We see that all the normal stress components are compressive in the external pressure case.

Impact of Operating Conditions

We now discern the impact of external pressure, current density, surface roughness and ambient temperature on the electrodeposition stability at the Li metal-solid electrolyte interface cognizant of the kinetic-transport-stress coupling. From our discussion on external pressure considerations, we have been able to deduce the relatively small impact of stress on the reaction current density. This allows us to decouple the stress and surface overpotential terms which can now be estimated separately to delineate the electrodeposition stability. The electrolyte potential difference, $\Delta\phi_e$, between the peak and the valley can be calculated using ion-transport considerations⁸⁸,

$$\Delta\phi_e = \frac{S_R i_{app}}{\kappa_{SE}^{eff}} \quad (28)$$

The peak and valley surface overpotentials, η_p and η_v respectively, can then be estimated using the following equations

$$\eta_v = \frac{2RT}{F} \ln \left(m + \sqrt{1+m^2} \right), \quad m = \frac{i_{app}}{2i_0} \quad (29)$$

$$\eta_p = \eta_v + \Delta\phi_e \quad (30)$$

Finally, the electrodeposition stability parameter, i_p / i_v , is given by

$$\frac{i_p}{i_v} = \frac{\exp\left(\frac{1-\alpha_a}{RT}\mu_{e^-,p}\right)}{\exp\left(\frac{1-\alpha_a}{RT}\mu_{e^-,v}\right)} \cdot \left[\frac{\exp\left(\frac{\alpha_a F}{RT}\eta_p\right) - \exp\left(\frac{\alpha_a F}{RT}\eta_p\right)}{\exp\left(\frac{\alpha_a F}{RT}\eta_v\right) - \exp\left(\frac{\alpha_a F}{RT}\eta_v\right)} \right] = I_s \cdot I_t$$

(31)

$$0.99 < I_s < 1.01, I_t > 1$$

Here, I_s denotes the stress contributions to the electrodeposition stability and I_t denotes the combined ionic transport and reaction overpotential contribution to the electrodeposition stability parameter. It is noteworthy that while external pressure-based stress effects can increase/decrease the deposition stability depending on the shear modulus and molar volume ratio values in a small window, ion transport effects will always contribute to a higher current density at the peak as compared to the valley.

Figure 5(a) delineates the impact of external pressure on electrodeposition stability parameter as a function of the SE to Li metal shear modulus and molar volume ratio. The shear modulus ratio is screened from 0.01 to 2.0 while the molar volume ratio is screened from 0 to 4. While changing the shear modulus and molar volume ratios, the Li metal electrode shear modulus, Poisson's ratio and molar volume are kept constant to its intrinsic properties: 3.4 GPa, 0.42 and 1.3×10^{-5} m³/mol respectively. Table 1 lists the mechanical, transport and kinetic parameters for the Li metal and the solid electrolyte system. Here, we take the electrochemical properties to be that of the inorganic LLZO system i.e. ionic conductivity and exchange current density are 0.10 S/m and 5.5 A/m² respectively at base temperature of 25°C. The surface roughness is set to 500 nm, current density is 1 mA/cm² and operating temperature is 25°C. As we go from top to bottom, the external pressure is increased from 0.1 MPa to 100.0 MPa. At low pressures of 0.1 MPa and 1.0 MPa, the stress induced chemical potential change is insufficient to compensate for transport instability resulting in unstable deposition ($i_p/i_v > 1$) over the entire range of shear modulus and molar volume ratio. On further increase of the

external pressure to 10.0 MPa and 100.0 MPa we see a demarcation of the stable and unstable zones. As the external pressure is increased, the stress induced deposition stability improves trumping the instability caused by transport for very low shear modulus ratio. For 100.0 MPa external pressure, almost the entire range of molar volume ratio moves to stable deposition regime only for low shear modulus ratio. For high shear modulus ratio, unstable deposition ($i_p/i_v > 1$) is seen even at high pressures (≥ 10 MPa) which exemplifies that the transport effects due to the surface perturbation cause the current to focus on the peak rather than the valley and stress is unable to redirect the flux away from the peak. We reiterate that transport always causes current instability, while external pressure induced interfacial stress (which is a function of the shear modulus and molar volume ratio) impacts the reaction kinetics. From the results, this impact of stress on reaction kinetics can counteract the transport instability only for low shear modulus ratios at high pressures ≥ 10 MPa . For high shear modulus ratio, transport trumps kinetics and deposition is always unstable. An interesting observation is the monotonic decrease of deposition instability as we go towards lower molar volume ratios. The effect of molar volume is more prominent as opposed to the shear modulus ratio, evidenced by the larger colour gradient along the horizontal axis. Under external pressure considerations, we no longer see the non-monotonic trend of deposition stability as a function of the molar volume reported in Ahmad *et al.*⁵⁷ which predicts an inversion of electrodeposition stability beyond $V_{SE} / V_{Li} = 1$ stating that low shear modulus electrolytes for molar volume ratios < 1 and high shear modulus electrolytes for molar volume ratios > 1 are inherently stable . In literature, the molar volume of inorganic SE has been proposed to be zero or close to zero^{22, 57-58}; in this regime, we see that it is hard to maintain stable deposition at high shear modulus ratios. It is evident that even as high as $G_{SE} / G_{Li} = 50$ or 100, deposition is unstable.

We see that under megapascal external pressure considerations we get contrasting results as compared to that given by Monroe-Newman theory where stresses are of the order of gigapascals. As the external pressure is increased, deposition stability is increased in low shear modulus ratio, on the other hands, deposition stability is decreased in high shear modulus ratio. Whereas, in literature, stiffer solid electrolytes with shear modulus more than twice that of Li metal have been proposed to suppress dendrites. We hypothesize that this trend inversion in our study is a consequence of the compressive external pressure considerations where the normal stresses ($\sigma_{xx}, \sigma_{yy}, \sigma_{zz}$) are all compressive in nature all throughout the solid electrolyte and hence at the peak and valleys of the perturbation there is primarily compressive normal stress. Furthermore, shear stresses are an order of magnitude smaller as compared to the normal stress in the external pressure regime. For the 10 MPa and 100 MPa external pressure cases, the stresses are now large enough to have some impact on the reaction kinetics. Depending on the external pressure magnitude, the stable zone changes and larger stable zone is observed at higher pressures. In contrast, for zero displacement boundary conditions both tensile and compressive stresses at the interfacial peaks and valleys are observed and shear stresses exhibit large magnitudes as well.

Figure 5(b) underscores the impact of applied current density on the deposition stability. Here, the external pressure is set to 10 MPa, surface roughness is 500 nm and ambient temperature is 25°C. As the current density is increased from 0.1 mA/cm² to 10.0 mA/cm², the transport instabilities are exacerbated due to high current rate engendering a wide potential difference between the peaks and the valleys, $i_{app} \uparrow, \Delta\phi_e \uparrow$. The stable zone shrinks as the current density is increased; stress is unable to divert the lithium flux away from the Li protrusions. The magnitude of the instability increases beyond 1 at current densities above 5.0 mA/cm². This exemplifies that it is difficult to ensure stable deposition at high current densities

and provides a reasoning for the critical current density observations for solid electrolytes. As the current density keeps on increasing, the propensity of Li peaks to grow rapidly increases. Beyond a threshold current density, the Li peak will grow unhindered and can reach the cathode through the grain boundaries fracture causing an internal short and failure of the ASSB.

Figure 6(a) exhibits the impact of the surface roughness on deposition stability keeping external pressure at 10 MPa, applied current density at 1 mA/cm² and operating temperature at 25°C. As the surface roughness at the metal-electrolyte interface increases, the transport instabilities start to grow, $S_R \uparrow, \Delta\phi_e \uparrow$. The potential difference between the peak and the valley widens; increasing the transport instabilities. Interestingly, the stress effects can counter the transport instability rise at high molar volume ratios >2.5 only for very low shear modulus ratio. The hydrostatic and deviatoric stress contributions redirect the Li⁺ flux away from the peaks to the valleys at these ratios. For all molar volume ratios, the instability keeps on rising as the surface roughness is increased. As surface roughness is increased, the peak and the valley lie farther apart. Ion transport to the peak becomes more easier as opposed to the valley, and this transport exacerbation causes $i_p/i_v > 1$.

Finally, the impact of operating temperature on deposition stability is ascertained keeping the external pressure at 10 MPa, applied current density at 1 mA/cm² and surface roughness at 500 nm (see Figure 6(b)). The thermal environment is varied from 0°C to 60°C. It is evident that low temperature operation is unsuited for stable deposition. The decrease in ionic conductivity and exchange current density at low temperatures results in sluggish transport and kinetics creating a compounding effect. As the temperature is increased, enhancement of both these parameters result in smaller surface overpotential variation between the peak and the valley which can be countered by stress effects. The stable zone grows as we move towards higher operating temperatures. Clearly, the SE-Li metal system is aided by

thermal ramps. The flowability of the Li metal is also enhanced at high temperatures, improving contact area. A detailed insight into those effects requires elasto-plastic deformation of the Li metal as well incorporation of creep effects⁸⁹⁻⁹⁰.

Figures S2-S5 exhibit the impact of operating conditions (pressure, current density, surface roughness, and ambient temperature) on the deposition stability for solid electrolytes with electrochemical properties akin to amorphous and crystalline sulfide solid electrolyte. Figure S2-S3 pertains to the amorphous sulfide electrolyte which has higher ionic conductivity (0.04 S/m) as compared to crystalline solid electrolyte. Figure S4-S5 pertains to the crystalline solid electrolyte which has a lower ionic conductivity (0.03 S/m). It is evident that the deposition instability magnitudes are higher for the crystalline SE owing to its inferior ion conduction capabilities. Furthermore, we see that both amorphous and crystalline LPS exhibit unstable deposition over the shear moduli and molar volume ratio investigated for a pressure up to 10 MPa. Only at extremely high pressures (100 MPa), we see the delineation of a stable zone at large molar volume ratios. This further exemplifies that the impact of pressure on reaction kinetics for solid electrolytes is negligible for the general ranges in which experimental stack pressure lie (up to 10-15 MPa) and transport will always lead to higher current density at the peak as compared to valley for these inorganic solid electrolytes. Smooth surface (low amplitude of perturbation) and ionic conductivities more than 0.1 S/m are essential towards maintaining good performance of all solid-state batteries. The effect of pressure is hypothesized to ensure plastic flow and good conformal contact between the Li metal-solid electrolyte interface. There is negligible impact of pressure-based stress on the reaction kinetics at the interface in the range of stack pressures experimentally investigated. For model-based investigations of deposition characteristics at the Li metal-solid electrolyte under stack pressure below 10 MPa, it is the opinion of the authors to neglect the effect of stress induced electrochemical potential change at the interface.

Experimental Validation

The LPS solid electrolyte can also exist in amorphous as well as crystalline form. We performed experiments to tabulate the overpotential for the Li plating reaction for Li|Li symmetric cells with crystalline (symbol: circle) and amorphous LPS (symbol: square) operating under varying external pressure and ambient temperature and report it in Figure 7(a). For the two a-LPS systems, the stack pressure is kept the same at 1.5 MPa and operating temperature is kept at 60°C and 100°C respectively. For the two c-LPS systems, the operating temperature is kept the same at 100°C while the stack pressures are 1.5 MPa and 7.0 MPa respectively. Such a methodical variation helps in delineating the impact of external pressure and operating temperature individually. It must also be noted that the a-LPS system cannot withstand higher stack pressures beyond 1.5 MPa because of low fracture toughness ($0.3 \text{ MPa} \cdot \text{m}^{1/2}$) , hence we chose the above variation. We can see that the a-LPS system can be operated at higher critical current densities from 20 mA/cm² up to 30 mA/cm² when the operating temperature is increased from 60°C to 100°C. Furthermore, the operating overpotential decreases as the temperature is increased from 60°C to 100°C for the a-LPS system. At an applied current density of 15 mA/cm², the overpotential reduces from approximately 0.30 V to 0.02 V for a temperature change from 60°C to 100°C. These features show the advantage of high temperature operation. In comparison, the c-LPS system cannot work beyond a critical current density of 10 mA/cm² even at high stack pressures of 7 MPa and high operating temperature of 100°C. For the low stack pressure of 1.5MPa, the critical current density for the c-LPS system lies below 5 mA/cm². At an applied current density of 4 mA/cm², the overpotential of the 7.0 MPa stack pressure c-LPS lies below the 1.5 MPa stack pressure c-LPS, underlying the benefits of high pressure.

Table 1 lists the mechanical, transport and kinetic parameters for our experimental system. Surface roughness of the LPS solid electrolyte is measured using atomic force

microscopy (AFM) with crystalline LPS exhibiting roughness ranging from average value of 131 nm to maximum roughness 1300 nm. Amorphous LPS shows a smaller variability in the surface roughness with values from average of 20.2 nm to maximum of 96 nm. The obtained ionic conductivities of the amorphous and crystalline LPS are 0.04 S/m and 0.03 S/m respectively, with nearly 25% lower value of crystalline LPS conductivity attributable to the presence of voids and grain boundaries. The void percentage is close to 10% in the crystalline LPS (90% relative density) which reduces the effective ionic conductivity to 75% of its pristine value, which is also in accordance with our microstructure-based characterization (see Figure 3(a)). At 10% void fraction, Figure 3(a) shows that the effective ionic conductivity reduces to 80% of the intrinsic value, approximately close to our experimentally obtained value.

It is evident that the performance of a-LPS at 60°C under 1.5 MPa external pressure is overshadowed by its counterpart operation at 100°C. This is directly correlated to the enhancement of the ionic conductivity and exchange current density at higher temperatures. We hypothesise that high temperature also improves Li ductility and creep allowing for better area contact between the Li metal and solid electrolyte interface^{42, 90}. A further drop in overpotential is seen when the c-LPS at 100°C under 1.5 MPa external pressure is subjected to an increase in pressure to 7 MPa. High pressure increases the interfacial contact and can decrease the surface roughness of the Li metal as well, improving the performance^{52, 63}. We conduct deposition stability parameter computations for the c-LPS and a-LPS with average surface roughness 131.0 nm and 20.2 nm respectively, nominal conductivity of 0.03 mS/cm and 0.04 mS/cm respectively and exchange current density of 12.6 A/m². With temperature, the ionic conductivity and exchange current density show Arrhenius dependence with activation energies tabulated in Table 1. From the perspective of the deposition stability parameter, a qualitative match is obtained between the experiments and the numerical model for thermal effects shown in Figure 7(b). The current instability parameter is the largest for the

c-LPS at 7.0 MPa followed by the c-LPS at 1.5 MPa stack pressure operating at 100°C. The experimental results show lower overpotentials with higher pressure, we hypothesize that this is the consequence of contact area enhancement, which needs to be incorporated in deposition stability computations. Our simulations have not taken contact area increase under higher external pressure into account and will be the focus of next study. Operating temperature dataset shows a decrease in deposition instability as the operating temperature is increased from 60°C to 100°C at 1.5 MPa stack pressure for a-LPS. High temperature leads to smaller current instabilities which are hypothesized to correspond with smaller overpotentials. It is worthwhile to note that the current instability parameter magnitudes are larger for c-LPS as compared to a-LPS over all molar volume ratios investigated. This is a direct consequence of the higher ionic conductivity of a-LPS as compared to c-LPS ($0.04 \text{ S/m} > 0.03 \text{ S/m}$). Also, for the amorphous system since it is the temperature that is being varied and not the external pressure, we see instability profiles with similar slope for both the temperatures. We are correlating experimental voltage performance with current instability. While there is no direct quantitative link between calculated voltage and current instability, through this method we propose that there is a qualitative match between high instability and high overpotential. Molar volume impacts the current instability parameters through the stress magnitudes and since the stress is kept the same for a-LPS, the instability curves show nearly equal variation with molar volume. In contrast, the c-LPS current instability curves show different slopes as a function of molar volume due to the operation at different pressure of 1.5 MPa and 7.0 MPa.

The current model aims at providing a qualitative match with experiments through computation of the static current instability parameter as a function of external pressure and temperature. We are calculating static current instability parameter at different current densities, temperature and pressure and trying to correlate it with experimental voltage curves. We hypothesize that high current instability can lead to high overpotentials. The limitations of

this model include dynamic quantitative voltage computation with interfacial area evolution due to peeling, contact loss, Li ductility, creep and will be the focus of a dynamic paper with symmetric cell model. Also, it is to be noted here that symmetrical cell configuration is used in the experiments. The phenomena of deposition and/or dissolution of lithium metal can affect voltage change. The numerical calculation results are only for the case of deposition.

Conclusion

In summary, we have devised the optimal solid electrolyte microstructure with beneficial transport and mechanical characteristics. Polycrystalline and amorphous solid electrolyte microstructure with grain size in excess of 25 μm , porosity <5% and void size <2 μm provides the optimal ionic conductivity and stiffness. Further, we developed an analytical model to discern the stress-transport-electrochemistry coupling in the Li metal-solid electrolyte system under external pressure considerations. We revealed that the stress impact on reaction kinetics diminishes considerably in the presence of an external “stack” pressure as opposed to the zero displacement boundary conditions generally used in literature. Using linear elasticity perturbation theory, we developed an analytical formalism capable of predicting the electrodeposition stability at Li metal-SE interface under a wide range of operating conditions including external pressure, surface roughness, current density and ambient temperature. An argument can be made for neglecting the impact of stress on chemical potential in calculations of electrodeposition stability under external pressures less than 10 MPa. The experimental stack pressure magnitudes rarely go above this, so we hypothesize the improvement of performance at pressures in this range to the plastic deformation of Li metal improving the area contact. We provided a phase map for the stable regimes as a function of the SE to Li metal shear modulus ratio and SE to Li metal molar volume ratio. Interestingly, the stability regimes show enhanced deposition stability as we go towards high molar volume ratios and low shear modulus ratios.

For high current operations, we need to operate the cell under high external pressure > 10 MPa which smoothens out the interfacial perturbations to less than 100 nm utilizing a low shear modulus $G_{SE} / G_{Li} < 1$. We aimed at providing an analytical framework to predict the electrodeposition stability and consequently our model has its limitations with linear elastic assumption being the chief one. Li metal has extremely low yield stress (~0.4 MPa) which will lead to plastic flow of Li under the pressures investigated here. Nevertheless, since we already showed that stress has a negligible impact on the chemical potential change in the MPa range, we have a high degree of confidence in the applicability of our predictions from this simplified analytical model. The inclusion of Li ductility, creep under dynamic electrodeposition and stripping at the metal-solid electrolyte interface requires complex coupled numerical computational approaches, with significant progress being made in this direction^{62, 64}. From a modelling perspective, a holistic model including aforementioned physics should be able to predict Li metal-solid electrolyte interfacial area evolution (through plastic flow of Li electrodeposit under pressure and interfacial void formation under stripping) and provide a pathway towards predicting the optimal stack pressure for all solid state battery operation for a wide range of inorganic/organic solid electrolytes.

Conflicts of interest

There are no conflicts to declare.

Acknowledgements

This work was supported by Nissan Research Center, Nissan Motor Co., Ltd. Japan.

References

- (1) Tarascon, J.-M.; Armand, M. Issues and challenges facing rechargeable lithium batteries. In *Materials For Sustainable Energy: A Collection of Peer-Reviewed Research and Review Articles from Nature Publishing Group*; World Scientific: 2011; pp 171-179.

- (2) Peled, E.; Menachem, C.; Bar - Tow, D.; Melman, A. Improved Graphite Anode for Lithium - Ion Batteries Chemically Bonded Solid Electrolyte Interface and Nanochannel Formation. *Journal of The Electrochemical Society* **1996**, *143* (1), L4-L7.
- (3) Liu, S.; Xiong, L.; He, C. Long cycle life lithium ion battery with lithium nickel cobalt manganese oxide (NCM) cathode. *Journal of Power Sources* **2014**, *261*, 285-291.
- (4) Xu, W.; Wang, J.; Ding, F.; Chen, X.; Nasybulin, E.; Zhang, Y.; Zhang, J.-G. Lithium metal anodes for rechargeable batteries. *Energy & Environmental Science* **2014**, *7* (2), 513-537.
- (5) Wood, K. N.; Noked, M.; Dasgupta, N. P. Lithium metal anodes: toward an improved understanding of coupled morphological, electrochemical, and mechanical behavior. *ACS Energy Letters* **2017**, *2* (3), 664-672.
- (6) Chen, K.-H.; Wood, K. N.; Kazyak, E.; LePage, W. S.; Davis, A. L.; Sanchez, A. J.; Dasgupta, N. P. Dead lithium: mass transport effects on voltage, capacity, and failure of lithium metal anodes. *Journal of Materials Chemistry A* **2017**, *5* (23), 11671-11681.
- (7) Bai, P.; Li, J.; Brushett, F. R.; Bazant, M. Z. Transition of lithium growth mechanisms in liquid electrolytes. *Energy & Environmental Science* **2016**, *9* (10), 3221-3229.
- (8) Thangadurai, V.; Narayanan, S.; Pinzaru, D. Garnet-type solid-state fast Li ion conductors for Li batteries: critical review. *Chemical Society Reviews* **2014**, *43* (13), 4714-4727.
- (9) Chen, S.; Xie, D.; Liu, G.; Mwizerwa, J. P.; Zhang, Q.; Zhao, Y.; Xu, X.; Yao, X. Sulfide solid electrolytes for all-solid-state lithium batteries: structure, conductivity, stability and application. *Energy Storage Materials* **2018**, *14*, 58-74.
- (10) Fujimura, K.; Seko, A.; Koyama, Y.; Kuwabara, A.; Kishida, I.; Shitara, K.; Fisher, C. A.; Moriwake, H.; Tanaka, I. Accelerated Materials Design of Lithium Superionic Conductors Based on First - Principles Calculations and Machine Learning Algorithms. *Advanced Energy Materials* **2013**, *3* (8), 980-985.
- (11) Inaguma, Y.; Liquan, C.; Itoh, M.; Nakamura, T.; Uchida, T.; Ikuta, H.; Wakihara, M. High ionic conductivity in lithium lanthanum titanate. *Solid State Communications* **1993**, *86* (10), 689-693.
- (12) Bates, J.; Dudney, N.; Neudecker, B.; Ueda, A.; Evans, C. Thin-film lithium and lithium-ion batteries. *Solid State Ionics* **2000**, *135* (1), 33-45.
- (13) Dudney, N. J. Solid-state thin-film rechargeable batteries. *Materials Science and Engineering: B* **2005**, *116* (3), 245-249.
- (14) Murugan, R.; Thangadurai, V.; Weppner, W. Fast lithium ion conduction in garnet - type Li₇La₃Zr₂O₁₂. *Angewandte Chemie International Edition* **2007**, *46* (41), 7778-7781.
- (15) Kamaya, N.; Homma, K.; Yamakawa, Y.; Hirayama, M.; Kanno, R.; Yonemura, M.; Kamiyama, T.; Kato, Y.; Hama, S.; Kawamoto, K. A lithium superionic conductor. *Nature materials* **2011**, *10* (9), 682-686.
- (16) Hatzell, K. B.; Chen, X. C.; Cobb, C. L.; Dasgupta, N. P.; Dixit, M. B.; Marbella, L. E.; McDowell, M. T.; Mukherjee, P. P.; Verma, A.; Viswanathan, V. Challenges in lithium metal anodes for solid-state batteries. *ACS Energy Letters* **2020**, *5* (3), 922-934.
- (17) Luntz, A. C.; Voss, J.; Reuter, K., Interfacial challenges in solid-state Li ion batteries. ACS Publications: 2015.
- (18) Basappa, R. H.; Ito, T.; Yamada, H. Contact between garnet-type solid electrolyte and lithium metal anode: influence on charge transfer resistance and short circuit prevention. *Journal of The Electrochemical Society* **2017**, *164* (4), A666-A671.
- (19) Santhanagopalan, D.; Qian, D.; McGilvray, T.; Wang, Z.; Wang, F.; Camino, F.; Graetz, J.; Dudney, N.; Meng, Y. S. Interface limited lithium transport in solid-state batteries. *The journal of physical chemistry letters* **2013**, *5* (2), 298-303.
- (20) Zhu, Y.; He, X.; Mo, Y. First principles study on electrochemical and chemical stability of solid electrolyte-electrode interfaces in all-solid-state Li-ion batteries. *Journal of Materials Chemistry A* **2016**, *4* (9), 3253-3266.
- (21) Fleig, J.; Maier, J. The impedance of imperfect electrode contacts on solid electrolytes. *Solid State Ionics* **1996**, *85* (1-4), 17-24.

- (22) Barai, P.; Higa, K.; Ngo, A. T.; Curtiss, L. A.; Srinivasan, V. Mechanical Stress Induced Current Focusing and Fracture in Grain Boundaries. *Journal of The Electrochemical Society* **2019**, *166* (10), A1752-A1762.
- (23) Bucci, G.; Swamy, T.; Chiang, Y.-M.; Carter, W. C. Modeling of internal mechanical failure of all-solid-state batteries during electrochemical cycling, and implications for battery design. *Journal of Materials Chemistry A* **2017**, *5* (36), 19422-19430.
- (24) Koerver, R.; Zhang, W.; de Biasi, L.; Schweiidler, S.; Kondrakov, A. O.; Kolling, S.; Brezesinski, T.; Hartmann, P.; Zeier, W. G.; Janek, J. Chemo-mechanical expansion of lithium electrode materials—on the route to mechanically optimized all-solid-state batteries. *Energy & Environmental Science* **2018**, *11* (8), 2142-2158.
- (25) Harry, K. J.; Hallinan, D. T.; Parkinson, D. Y.; MacDowell, A. A.; Balsara, N. P. Detection of subsurface structures underneath dendrites formed on cycled lithium metal electrodes. *Nature materials* **2014**, *13* (1), 69-73.
- (26) Harry, K. J.; Higa, K.; Srinivasan, V.; Balsara, N. P. Influence of electrolyte modulus on the local current density at a dendrite tip on a lithium metal electrode. *Journal of The Electrochemical Society* **2016**, *163* (10), A2216-A2224.
- (27) Maslyn, J. A.; Loo, W. S.; McEntush, K. D.; Oh, H. J.; Harry, K. J.; Parkinson, D. Y.; Balsara, N. P. Growth of lithium dendrites and globules through a solid block copolymer electrolyte as a function of current density. *The Journal of Physical Chemistry C* **2018**, *122* (47), 26797-26804.
- (28) Barai, P.; Higa, K.; Srinivasan, V. Impact of external pressure and electrolyte transport properties on lithium dendrite growth. *Journal of The Electrochemical Society* **2018**, *165* (11), A2654-A2666.
- (29) Cheng, L.; Chen, W.; Kunz, M.; Persson, K.; Tamura, N.; Chen, G.; Doeff, M. Effect of surface microstructure on electrochemical performance of garnet solid electrolytes. *ACS applied materials & interfaces* **2015**, *7* (3), 2073-2081.
- (30) Fu, K. K.; Gong, Y.; Dai, J.; Gong, A.; Han, X.; Yao, Y.; Wang, C.; Wang, Y.; Chen, Y.; Yan, C. Flexible, solid-state, ion-conducting membrane with 3D garnet nanofiber networks for lithium batteries. *Proceedings of the National Academy of Sciences* **2016**, *113* (26), 7094-7099.
- (31) Park, K.; Yu, B.-C.; Jung, J.-W.; Li, Y.; Zhou, W.; Gao, H.; Son, S.; Goodenough, J. B. Electrochemical nature of the cathode interface for a solid-state lithium-ion battery: interface between LiCoO₂ and garnet-Li₇La₃Zr₂O₁₂. *Chemistry of Materials* **2016**, *28* (21), 8051-8059.
- (32) Fu, K.; Gong, Y.; Fu, Z.; Xie, H.; Yao, Y.; Liu, B.; Carter, M.; Wachsman, E.; Hu, L. Transient behavior of the metal interface in lithium metal–garnet batteries. *Angewandte Chemie International Edition* **2017**, *56* (47), 14942-14947.
- (33) Swamy, T.; Park, R.; Sheldon, B. W.; Rettenwander, D.; Porz, L.; Berendts, S.; Uecker, R.; Carter, W. C.; Chiang, Y.-M. Lithium metal penetration induced by electrodeposition through solid electrolytes: example in single-crystal Li₆La₃ZrTaO₁₂ garnet. *Journal of The Electrochemical Society* **2018**, *165* (16), A3648.
- (34) Han, X.; Gong, Y.; Fu, K. K.; He, X.; Hitz, G. T.; Dai, J.; Pearse, A.; Liu, B.; Wang, H.; Rubloff, G. Negating interfacial impedance in garnet-based solid-state Li metal batteries. *Nature materials* **2017**, *16* (5), 572-579.
- (35) Lau, J.; DeBlock, R. H.; Butts, D. M.; Ashby, D. S.; Choi, C. S.; Dunn, B. S. Sulfide solid electrolytes for lithium battery applications. *Advanced Energy Materials* **2018**, *8* (27), 1800933.
- (36) Yu, C.; Ganapathy, S.; de Klerk, N. J.; Roslon, I.; van Eck, E. R.; Kentgens, A. P.; Wagemaker, M. Unravelling li-ion transport from picoseconds to seconds: bulk versus interfaces in an argyrodite Li₆P₅Cl₆-Li₂S all-solid-state li-ion battery. *Journal of the American Chemical Society* **2016**, *138* (35), 11192-11201.
- (37) Zhang, Z.; Chen, S.; Yang, J.; Wang, J.; Yao, L.; Yao, X.; Cui, P.; Xu, X. Interface re-engineering of Li₁₀GeP₂S₁₂ electrolyte and lithium anode for all-solid-state lithium batteries with ultralong cycle life. *ACS applied materials & interfaces* **2018**, *10* (3), 2556-2565.
- (38) Famprakis, T.; Canepa, P.; Dawson, J. A.; Islam, M. S.; Masquelier, C. Fundamentals of inorganic solid-state electrolytes for batteries. *Nature materials* **2019**, 1-14.

- (39) Jung, Y. S.; Oh, D. Y.; Nam, Y. J.; Park, K. H. Issues and challenges for bulk - type all - solid - state rechargeable lithium batteries using sulfide solid electrolytes. *Israel Journal of Chemistry* **2015**, 55 (5), 472-485.
- (40) Tatsumisago, M.; Mizuno, F.; Hayashi, A. All-solid-state lithium secondary batteries using sulfide-based glass-ceramic electrolytes. *Journal of power sources* **2006**, 159 (1), 193-199.
- (41) Ni, J. E.; Case, E. D.; Sakamoto, J. S.; Rangasamy, E.; Wolfenstine, J. B. Room temperature elastic moduli and Vickers hardness of hot-pressed LLZO cubic garnet. *Journal of Materials Science* **2012**, 47 (23), 7978-7985.
- (42) Sharafi, A.; Meyer, H. M.; Nanda, J.; Wolfenstine, J.; Sakamoto, J. Characterizing the Li-Li₇La₃Zr₂O₁₂ interface stability and kinetics as a function of temperature and current density. *Journal of Power Sources* **2016**, 302, 135-139.
- (43) Cheng, E. J.; Sharafi, A.; Sakamoto, J. Intergranular Li metal propagation through polycrystalline Li₆.25Al₀.25La₃Zr₂O₁₂ ceramic electrolyte. *Electrochimica Acta* **2017**, 223, 85-91.
- (44) Porz, L.; Swamy, T.; Sheldon, B. W.; Rettenwander, D.; Frömling, T.; Thaman, H. L.; Berendts, S.; Uecker, R.; Carter, W. C.; Chiang, Y. M. Mechanism of lithium metal penetration through inorganic solid electrolytes. *Advanced Energy Materials* **2017**, 7 (20), 1701003.
- (45) Luo, W.; Gong, Y.; Zhu, Y.; Fu, K. K.; Dai, J.; Lacey, S. D.; Wang, C.; Liu, B.; Han, X.; Mo, Y. Transition from superlithiophobicity to superlithiophilicity of garnet solid-state electrolyte. *Journal of the American Chemical Society* **2016**, 138 (37), 12258-12262.
- (46) Luo, W.; Gong, Y.; Zhu, Y.; Li, Y.; Yao, Y.; Zhang, Y.; Fu, K.; Pastel, G.; Lin, C. F.; Mo, Y. Reducing interfacial resistance between garnet - structured solid - state electrolyte and Li - metal anode by a germanium layer. *Advanced Materials* **2017**, 29 (22), 1606042.
- (47) Shao, Y.; Wang, H.; Gong, Z.; Wang, D.; Zheng, B.; Zhu, J.; Lu, Y.; Hu, Y.-S.; Guo, X.; Li, H. Drawing a soft interface: an effective interfacial modification strategy for garnet-type solid-state Li batteries. *ACS Energy Letters* **2018**, 3 (6), 1212-1218.
- (48) Liu, B.; Gong, Y.; Fu, K.; Han, X.; Yao, Y.; Pastel, G.; Yang, C.; Xie, H.; Wachsman, E. D.; Hu, L. Garnet solid electrolyte protected Li-metal batteries. *ACS applied materials & interfaces* **2017**, 9 (22), 18809-18815.
- (49) Tsai, C.-L.; Roddatis, V.; Chandran, C. V.; Ma, Q.; Uhlenbruck, S.; Bram, M.; Heitjans, P.; Guillou, O. Li₇La₃Zr₂O₁₂ interface modification for Li dendrite prevention. *ACS applied materials & interfaces* **2016**, 8 (16), 10617-10626.
- (50) Van Den Broek, J.; Afyon, S.; Rupp, J. L. Interface - Engineered All - Solid - State Li - Ion Batteries Based on Garnet - Type Fast Li⁺ Conductors. *Advanced Energy Materials* **2016**, 6 (19), 1600736.
- (51) Jow, T.; Liang, C. Interface between solid anode and solid electrolyte-effect of pressure on Li/Li₂(Al₂O₃) interface. *Solid State Ionics* **1983**, 9, 695-698.
- (52) Wang, M. J.; Choudhury, R.; Sakamoto, J. Characterizing the Li-Solid-Electrolyte Interface Dynamics as a Function of Stack Pressure and Current Density. *Joule* **2019**, 3 (9), 2165-2178.
- (53) Kerman, K.; Luntz, A.; Viswanathan, V.; Chiang, Y.-M.; Chen, Z. practical challenges hindering the development of solid state Li ion batteries. *Journal of The Electrochemical Society* **2017**, 164 (7), A1731.
- (54) Monroe, C.; Newman, J. The effect of interfacial deformation on electrodeposition kinetics. *Journal of The Electrochemical Society* **2004**, 151 (6), A880-A886.
- (55) Monroe, C.; Newman, J. The impact of elastic deformation on deposition kinetics at lithium/polymer interfaces. *Journal of The Electrochemical Society* **2005**, 152 (2), A396-A404.
- (56) Barai, P.; Higa, K.; Srinivasan, V. Lithium dendrite growth mechanisms in polymer electrolytes and prevention strategies. *Physical Chemistry Chemical Physics* **2017**, 19 (31), 20493-20505.
- (57) Ahmad, Z.; Viswanathan, V. Stability of electrodeposition at solid-solid interfaces and implications for metal anodes. *arXiv preprint arXiv:1702.08406* **2017**.
- (58) Ahmad, Z.; Viswanathan, V. Role of anisotropy in determining stability of electrodeposition at solid-solid interfaces. *Physical Review Materials* **2017**, 1 (5), 055403.

- (59) Barai, P.; Ngo, A.; Narayanan, B.; Higa, K.; Curtiss, L. A.; Srinivasan, V. The role of local inhomogeneities on dendrite growth in LLZO-based solid electrolytes. *Journal of the Electrochemical Society* **2020**.
- (60) Sharafi, A.; Haslam, C. G.; Kerns, R. D.; Wolfenstine, J.; Sakamoto, J. Controlling and correlating the effect of grain size with the mechanical and electrochemical properties of Li₇La₃Zr₂O₁₂ solid-state electrolyte. *Journal of Materials Chemistry A* **2017**, 5 (40), 21491-21504.
- (61) Qingsong, T.; Luis, B.-L.; Tan, S.; Gerbrand, C. Modeling of Electro-deposition and Mechanical Stability at Li Metal/Solid Electrolyte Interface during Plating in Solid-State Batteries. *arXiv preprint arXiv:1910.13922* **2019**.
- (62) Zhang, X.; Wang, Q. J.; Harrison, K. L.; Roberts, S. A.; Harris, S. J. Pressure-Driven Interface Evolution in Solid-State Lithium Metal Batteries. *Cell Reports Physical Science* **2020**, 1 (2), 100012.
- (63) Zhang, X.; Wang, Q. J.; Harrison, K. L.; Jungjohann, K.; Boyce, B. L.; Roberts, S. A.; Attia, P. M.; Harris, S. J. Rethinking How External Pressure Can Suppress Dendrites in Lithium Metal Batteries. *Journal of The Electrochemical Society* **2019**, 166 (15), A3639-A3652.
- (64) Narayan, S.; Anand, L. On Modeling the Detrimental Effects of Inhomogeneous Plating-and-Stripping at a Lithium-Metal/Solid-Electrolyte Interface in a Solid-State-Battery. *Journal of The Electrochemical Society* **2020**, 167 (4), 040525.
- (65) Klinsmann, M.; Hildebrand, F. E.; Ganser, M.; McMeeking, R. M. Dendritic cracking in solid electrolytes driven by lithium insertion. *Journal of Power Sources* **2019**, 442, 227226.
- (66) Bucci, G.; Christensen, J. Modeling of lithium electrodeposition at the lithium/ceramic electrolyte interface: The role of interfacial resistance and surface defects. *Journal of Power Sources* **2019**, 441, 227186.
- (67) Mistry, A. N.; Mukherjee, P. P. Molar Volume Mismatch: a Malefactor for Irregular Metallic Electrodeposition with Solid Electrolytes. *Journal of the Electrochemical Society* **2020**.
- (68) Barroso-Luque, L.; Tu, Q.; Ceder, G. An Analysis of Solid-State Electrodeposition-Induced Metal Plastic Flow and Predictions of Stress States in Solid Ionic Conductor Defects. *Journal of The Electrochemical Society* **2020**, 167 (2), 020534.
- (69) Timoshenko, S. P.; Gere, J. M. *Theory of elastic stability*, Courier Corporation: 2009.
- (70) Tikekar, M. D.; Archer, L. A.; Koch, D. L. Stability analysis of electrodeposition across a structured electrolyte with immobilized anions. *Journal of The Electrochemical Society* **2014**, 161 (6), A847-A855.
- (71) McMeeking, R. M.; Ganser, M.; Klinsmann, M.; Hildebrand, F. E. Metal electrode surfaces can roughen despite the constraint of a stiff electrolyte. *Journal of The Electrochemical Society* **2019**, 166 (6), A984-A995.
- (72) Choudhury, S. Confining electrodeposition of metals in structured electrolytes. In *Rational Design of Nanostructured Polymer Electrolytes and Solid–Liquid Interphases for Lithium Batteries*; Springer: 2019; pp 59-79.
- (73) Cheng, L.; Park, J. S.; Hou, H.; Zorba, V.; Chen, G.; Richardson, T.; Cabana, J.; Russo, R.; Doeff, M. Effect of microstructure and surface impurity segregation on the electrical and electrochemical properties of dense Al-substituted Li₇La₃Zr₂O₁₂. *Journal of Materials Chemistry A* **2014**, 2 (1), 172-181.
- (74) David, I. N.; Thompson, T.; Wolfenstine, J.; Allen, J. L.; Sakamoto, J. Microstructure and Li - Ion Conductivity of Hot - Pressed Cubic Li₇La₃Zr₂O₁₂. *Journal of the American Ceramic Society* **2015**, 98 (4), 1209-1214.
- (75) Groeber, M. A.; Jackson, M. A. DREAM. 3D: a digital representation environment for the analysis of microstructure in 3D. *Integrating materials and manufacturing innovation* **2014**, 3 (1), 5.
- (76) Lacaille, V.; Morel, C.; Feulvarch, E.; Kermouche, G.; Bergheau, J.-M. Finite element analysis of the grain size effect on diffusion in polycrystalline materials. *Computational materials science* **2014**, 95, 187-191.
- (77) Yu, S.; Siegel, D. J. Grain boundary contributions to Li-ion transport in the solid electrolyte Li₇La₃Zr₂O₁₂ (LLZO). *Chemistry of Materials* **2017**, 29 (22), 9639-9647.

- (78) Dawson, J. A.; Canepa, P.; Famprakis, T.; Masquelier, C.; Islam, M. S. Atomic-scale influence of grain boundaries on Li-ion conduction in solid electrolytes for all-solid-state batteries. *Journal of the American Chemical Society* **2018**, *140* (1), 362-368.
- (79) Tenhaeff, W. E.; Rangasamy, E.; Wang, Y.; Sokolov, A. P.; Wolfenstine, J.; Sakamoto, J.; Dudney, N. J. Resolving the Grain Boundary and Lattice Impedance of Hot - Pressed Li₇La₃Zr₂O₁₂ Garnet Electrolytes. *ChemElectroChem* **2014**, *1* (2), 375-378.
- (80) Han, F.; Westover, A. S.; Yue, J.; Fan, X.; Wang, F.; Chi, M.; Leonard, D. N.; Dudney, N. J.; Wang, H.; Wang, C. High electronic conductivity as the origin of lithium dendrite formation within solid electrolytes. *Nature Energy* **2019**, *4* (3), 187-196.
- (81) Yu, S.; Siegel, D. J. Grain boundary softening: A potential mechanism for lithium metal penetration through stiff solid electrolytes. *ACS applied materials & interfaces* **2018**, *10* (44), 38151-38158.
- (82) Vargas - Barbosa, N. M.; Roling, B. Dynamic Ion Correlations in Solid and Liquid Electrolytes: How Do They Affect Charge and Mass Transport? *ChemElectroChem* **2019**.
- (83) Knauth, P. Inorganic solid Li ion conductors: An overview. *Solid State Ionics* **2009**, *180* (14-16), 911-916.
- (84) Srolovitz, D. J. On the stability of surfaces of stressed solids. *Acta metallurgica* **1989**, *37* (2), 621-625.
- (85) Angheluta, L.; Jettestuen, E.; Mathiesen, J. Thermodynamics and roughening of solid-solid interfaces. *Physical Review E* **2009**, *79* (3), 031601.
- (86) Shen, F.; Dixit, M. B.; Xiao, X.; Hatzell, K. B. Effect of pore connectivity on Li dendrite propagation within LLZO electrolytes observed with synchrotron X-ray tomography. *ACS Energy Letters* **2018**, *3* (4), 1056-1061.
- (87) Tu, Q.; Barroso-Luque, L.; Shi, T.; Ceder, G. Electrodeposition and Mechanical Stability at Lithium-Solid Electrolyte Interface during Plating in Solid-State Batteries. *Cell Reports Physical Science* **2020**, *100106*.
- (88) Akolkar, R. Mathematical model of the dendritic growth during lithium electrodeposition. *Journal of Power Sources* **2013**, *232*, 23-28.
- (89) Masias, A.; Felten, N.; Garcia-Mendez, R.; Wolfenstine, J.; Sakamoto, J. Elastic, plastic, and creep mechanical properties of lithium metal. *Journal of materials science* **2019**, *54* (3), 2585-2600.
- (90) LePage, W. S.; Chen, Y.; Kazyak, E.; Chen, K.-H.; Sanchez, A. J.; Poli, A.; Arruda, E. M.; Thouless, M.; Dasgupta, N. P. Lithium mechanics: roles of strain rate and temperature and implications for lithium metal batteries. *Journal of The Electrochemical Society* **2019**, *166* (2), A89-A97.
- (91) Sakuda, A.; Hayashi, A.; Takigawa, Y.; Higashi, K.; Tatsumisago, M. Evaluation of elastic modulus of Li₂S-P₂S₅ glassy solid electrolyte by ultrasonic sound velocity measurement and compression test. *Journal of the Ceramic Society of Japan* **2013**, *121* (1419), 946-949.

List of Tables:

Table 1 List of mechanical, transport and kinetic parameters

List of Figures:

Fig. 1. Schematic of the Li metal-solid electrolyte domain with a sinusoidal interfacial perturbation and perfect contact (left). Peaks and valleys correspond to the surface roughness of the metal-solid electrolyte domain. Current density from the counter electrode, i_{app} , redistributes through the polycrystalline/amorphous (right) solid electrolyte domain reaching the metal-electrolyte interface where the reduction of Li⁺ ions to metallic lithium occurs. An interfacial current density distribution governed by the coupled electrolyte transport, interfacial curvature and external pressure induced interfacial stress is established. Stability descriptor,

i_{peak} / i_{valley} , is used to distinguish the deposition regimes; i_{peak} and i_{valley} are the normal current densities at the peak and valley respectively. $i_{peak} / i_{valley} > 1$ implies preferential growth of the Li peaks as opposed to valleys (unstable deposition) and $i_{peak} / i_{valley} \leq 1$ corresponds to eventual flattening of the perturbation (stable deposition).

Fig. 2. Visualization of solid electrolyte (SE) microstructure with grains, grain boundaries and voids. (a-i) Polycrystalline SE without voids and grain size 10 μm . (a-ii) Polycrystalline SE with voids of size 4 μm , porosity 20% and grain size 20 μm . (b) Front view of polycrystalline SE with varying grain size, void size and void fraction. (b-i) 5 μm – 4 μm – 5%, (b-ii) 10 μm – 4 μm – 5%, (b-iii) 5 μm – 10 μm – 5% and (d) 5 μm – 4 μm – 20%. As the grain size increases, grain boundary density decreases. As void size increases, number of voids for the same void volume decreases. (c) Front view of amorphous SE with varying void size and void fraction. (c-i) 4 μm - 5%, (c-ii) 10 μm – 5%, (c-iii) 4 μm – 20%. There are no grain boundaries in amorphous SE.

Fig. 3. Effective transport and mechanical property computations for the polycrystalline solid electrolyte system. (a), (c) and (e) exhibit the effective ionic conductivity, κ^{eff} , and (b), (d) and (f) show the effective Young's modulus, E^{eff} , as a function of grain size, porosity, grain boundary thickness, δ , and void size. (a), (b) Effective property variation with grain size and porosity for $\delta = 10\text{ nm}$. Rapid decrease in κ^{eff} and E^{eff} is seen with porosity increase while grain size has a relatively smaller impact. As grain size increases, the grain boundary density decreases resulting in enhanced transport, mechanics. (c), (d) Effective property variation with grain size and porosity for $\delta = 100\text{ nm}$. As grain boundary thickness increases, it occupies more volume and impedes transport further. (e), (f) Effective property variation with void size and porosity for $\delta = 10\text{ nm}$. Void size has negligible impact on effective properties.

Fig. 4. Stress contours in the Li metal (bottom) – solid electrolyte (top) domain for varying boundary conditions and interfacial perturbation amplitude, A . The interfacial perturbation is shown by a white line in the σ_{yy} contour plot. Li metal peaks are at $x = 0\text{ }\mu\text{m}$ and $x = 100\text{ }\mu\text{m}$ and valley at $x = 50\text{ }\mu\text{m}$. (a) Normal and shear stress for zero displacement boundary condition and $A = 1\mu\text{m}$. The stress magnitudes come in the range of gigapascals. (b) Normal and shear stress for external pressure boundary condition ($P_{ext} = 10\text{ MPa}$) and $S_R = 1\text{ nm}$ corresponding to a flat interface. σ_{yy} becomes equal to external pressure and shear stress tends to zero. (c) Normal and shear stress for external pressure boundary condition ($P_{ext} = 10\text{ MPa}$) and $S_R = 1\mu\text{m}$. With external pressure, the stresses inside the system lie in the megapascal range, nearly three orders of magnitude smaller as compared to zero displacement boundary condition. Stress impact on reaction kinetics gets reduced considerably.

Fig. 5. (a) Impact of external pressure and (b) current density on deposition stability as a function of the shear modulus and molar volume ratio for electrochemical properties of inorganic LLZO electrolyte (@ 25°C: $i_0 = 5.5\text{ A/m}^2$, $\kappa = 0.10\text{ S/m}$). As external pressure is increased, deposition stability improves across all molar volume ranges. As current density is increased, transport and kinetic overpotentials increase, resulting in stable deposition only at low current densities.

Fig. 6. (a) Impact of surface roughness and (b) temperature on deposition stability as a function of the shear modulus and molar volume ratio for electrochemical properties of inorganic LLZO electrolyte ($\text{@ } 25^\circ\text{C} : i_0 = 5.5 \text{ A/m}^2, \kappa = 0.10 \text{ S/m}$) . As surface roughness is increased, deposition instability magnitudes increase in the unstable zone. As temperature is decreased, transport and kinetic overpotentials increase, resulting in stable deposition only at high temperatures.

Fig. 7. Comparison between (a) experiments and (b) model for amorphous (a-LPS) and polycrystalline LPS (c-LPS) solid electrolyte. Amorphous LPS shows higher ionic conductivity ($0.4 > 0.3 \text{ mS/cm}$) and smaller average surface roughness ($20.2 < 131.0 \text{ nm}$) as compared to crystalline LPS. Amorphous LPS exhibits higher critical current densities and lower overpotentials as compared to crystalline LPS for same external pressure and temperature. As temperature increase, the deposition stability improves for all molar volume ratios investigated which can be correlated qualitatively with the overpotential decrease in symmetric cell experiments. An interesting result is that pressure increase results in more deposition instability from numerical computations for the LPS system investigated.

Tables and Table Captions:

Table 1. List of mechanical, transport and kinetic parameters

Name	Symbol	Unit	Value	Reference
Li Young's modulus	E_{Li}	GPa	9.0	²²
Li shear modulus	G_{Li}	GPa	3.4	²²
Li Poisson's ratio	ν_{Li}	-	0.42	²²
Li partial molar volume	V_{Li}	m^3/mol	1.3×10^{-5}	²²
LLZO Young's modulus	E_{LLZO}	GPa	150	²²
LLZO Poisson's ratio	ν_{LLZO}	-	0.20	²²
LLZO ionic conductivity	κ_{LLZO}	S/m	0.10	²²
LLZO exchange current density	$i_{0,LLZO}$	A/m^2	5.5	²²
Crystalline LPS Young's modulus	E_{LPS}	GPa	13	-
Amorphous LPS Young's modulus	E_{LPS}	GPa	11	-
LPS Poisson's ratio	ν_{LPS}	-	0.29	⁹¹

Crystalline LPS conductivity	κ_{c-LPS}	S/m	0.03	-
Amorphous LPS conductivity	κ_{a-LPS}	S/m	0.04	-
LPS exchange current density	$i_{0,LPS}$	A/m ²	12.6	-
Activation energy for electrolyte transport	$E_{a,\kappa}$	kJ/mol	15	-
Activation energy for charge transfer	E_{a,i_0}	kJ/mol	12	-

Figures and Figure Captions:

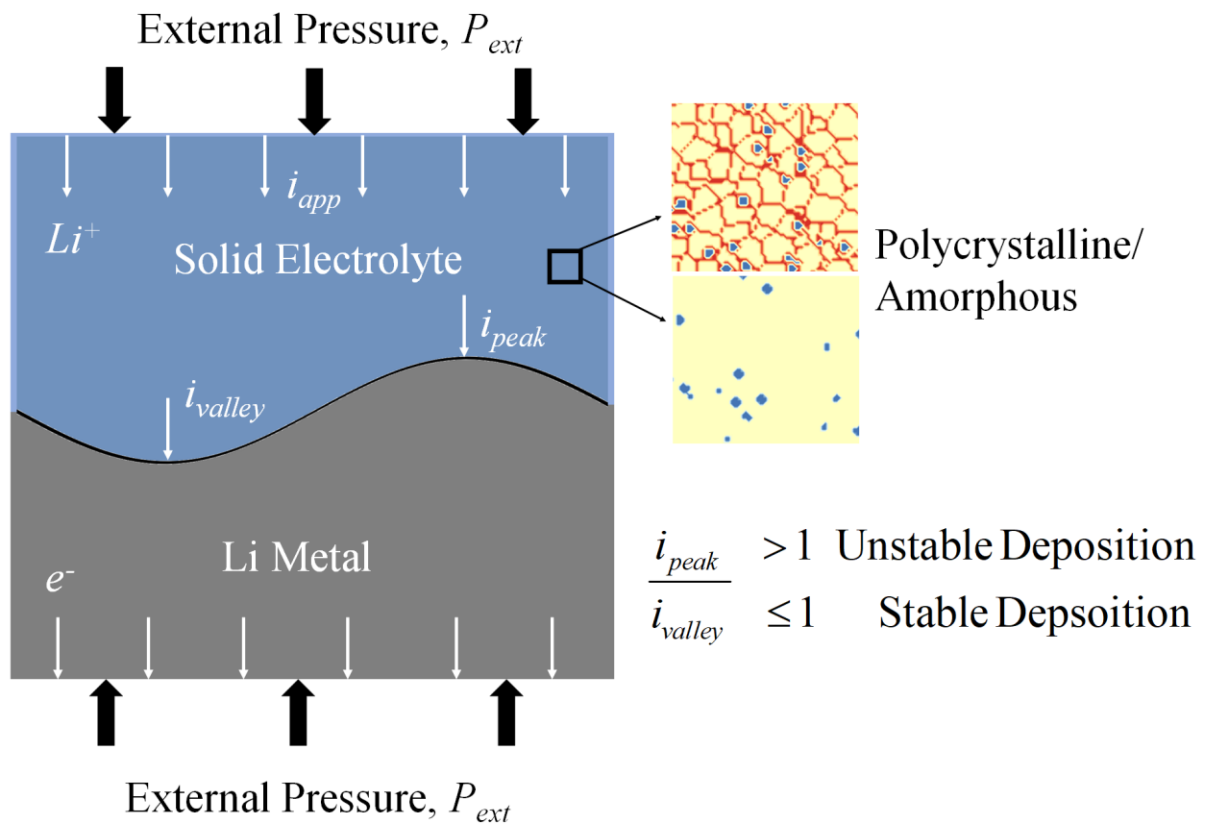


Fig. 1 Schematic of the Li metal-solid electrolyte domain with a sinusoidal interfacial perturbation and perfect contact (left). Peaks and valleys correspond to the surface roughness of the metal-solid electrolyte domain. Current density from the counter electrode, i_{app} , redistributes through the polycrystalline/amorphous (right) solid electrolyte domain reaching the metal-electrolyte interface where the reduction of Li^+ ions to metallic lithium occurs. An interfacial current density distribution governed by the coupled electrolyte transport, interfacial

curvature and external pressure induced interfacial stress is established. Stability descriptor, i_{peak} / i_{valley} , is used to distinguish the deposition regimes; i_{peak} and i_{valley} are the normal current densities at the peak and valley respectively. $i_{peak} / i_{valley} > 1$ implies preferential growth of the Li peaks as opposed to valleys (unstable deposition) and $i_{peak} / i_{valley} \leq 1$ corresponds to eventual flattening of the perturbation (stable deposition).

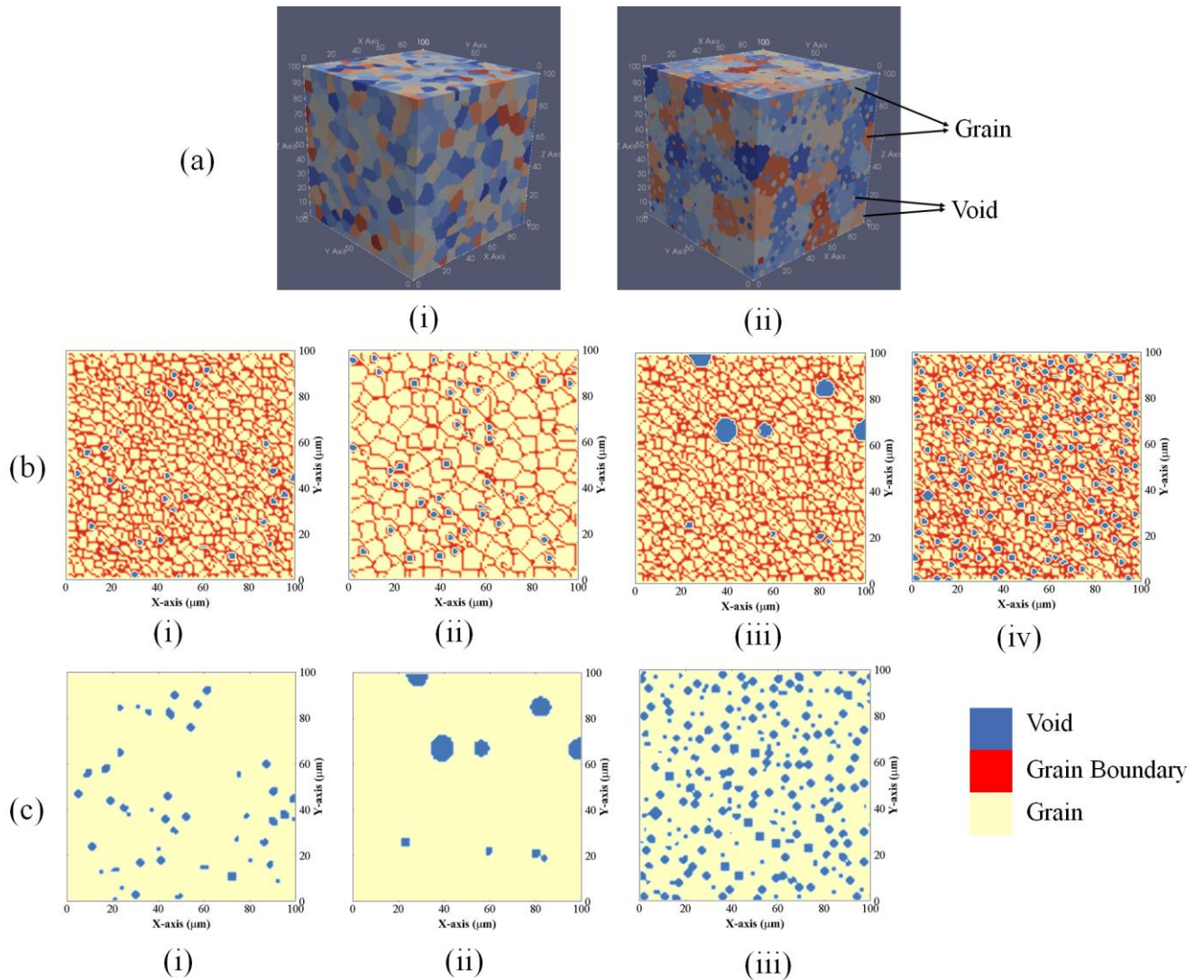


Fig. 2 Visualization of solid electrolyte (SE) microstructure with grains, grain boundaries and voids. (a-i) Polycrystalline SE without voids and grain size 10 μm . (a-ii) Polycrystalline SE with voids of size 5 μm and grain size 20 μm . (b) Front view of polycrystalline SE with varying grain size, void size and void fraction. (b-i) 5 μm – 4 μm – 5%, (b-ii) 10 μm – 4 μm – 5%, (b-iii) 5 μm – 10 μm – 5% and (d) 5 μm – 4 μm – 20%. As the grain size increases, grain boundary density decreases. As void size increases, number of voids for the same void volume decreases. (c) Front view of amorphous SE with varying void size and void fraction. (c-i) 4 μm - 5%, (c-ii) 10 μm – 5%, (c-iii) 4 μm – 20%. There are no grain boundaries in amorphous SE.

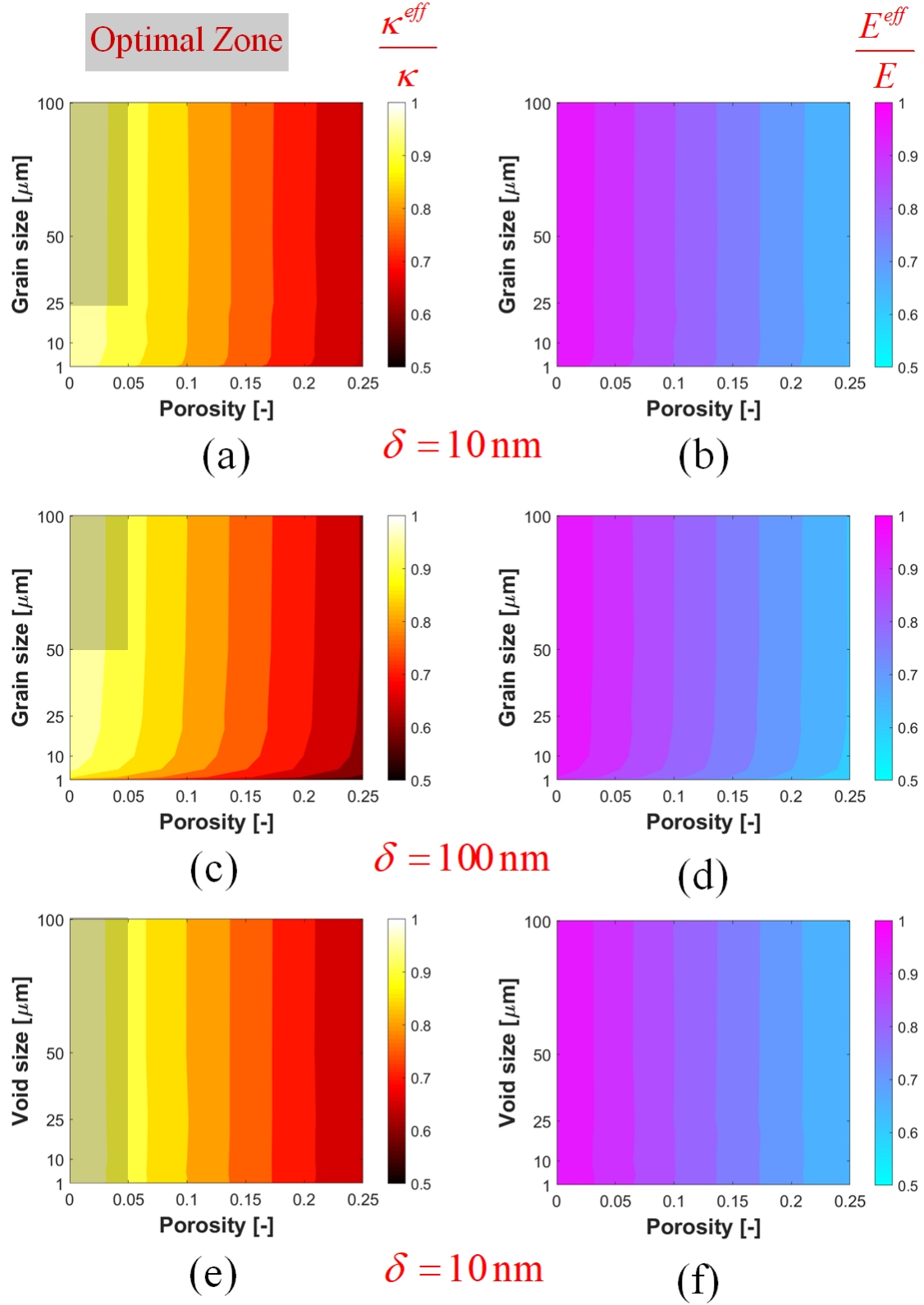


Fig. 3 Effective transport and mechanical property computations for the polycrystalline solid electrolyte system. (a), (c) and (e) exhibit the effective ionic conductivity, κ^{eff} , and (b), (d) and (f) show the effective Young's modulus, E^{eff} , as a function of grain size, porosity, grain boundary thickness, δ , and void size. (a), (b) Effective property variation with grain size and porosity for $\delta = 10\text{ nm}$. Rapid decrease in κ^{eff} and E^{eff} is seen with porosity increase while

grain size has a relatively smaller impact. As grain size increases, the grain boundary density decreases resulting in enhanced transport, mechanics. (c), (d) Effective property variation with grain size and porosity for $\delta = 100 \text{ nm}$. As grain boundary thickness increases, it occupies more volume and impedes transport further. (e), (f) Effective property variation with void size and porosity for $\delta = 10 \text{ nm}$. Void size has negligible impact on effective properties.

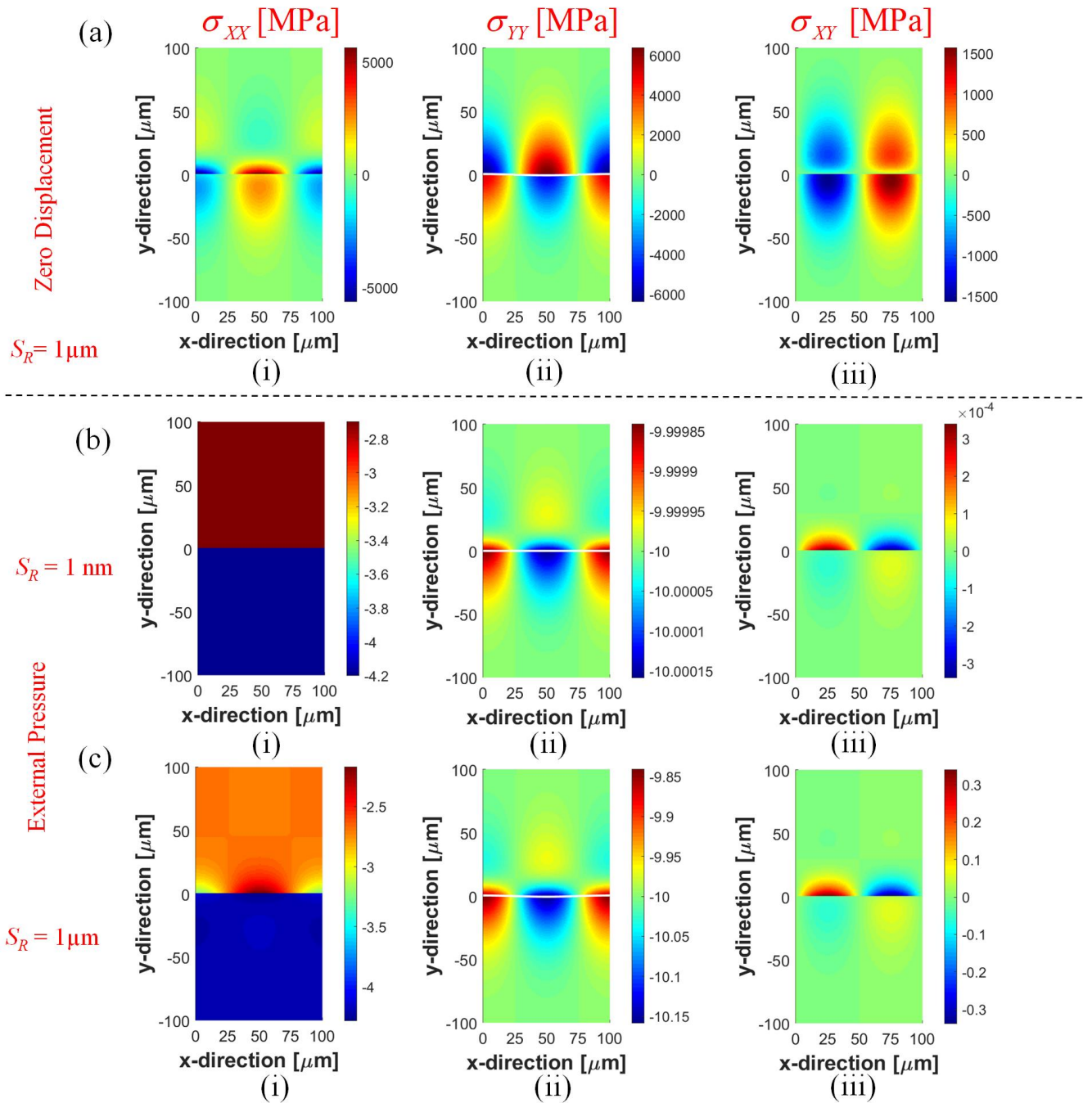


Fig. 4 Stress contours in the Li metal (bottom) – solid electrolyte (top) domain for varying boundary conditions and interfacial perturbation amplitude, A . The interfacial perturbation is shown by a white line in the σ_{YY} contour plot. Li metal peaks are at $x = 0 \mu\text{m}$ and $x = 100 \mu\text{m}$ and valley at $x = 50 \mu\text{m}$. (a) Normal and shear stress for zero displacement boundary condition and $A = 1\mu\text{m}$. The stress magnitudes come in the range of gigapascals. (b) Normal and shear stress for external pressure boundary condition ($P_{ext} = 10 \text{ MPa}$) and $S_R = 1\text{ nm}$ corresponding to a flat interface. σ_{YY} becomes equal to external pressure and shear stress tends to zero. (c) Normal and shear stress for external pressure boundary condition ($P_{ext} = 10 \text{ MPa}$) and

$S_R = 1\mu\text{m}$. With external pressure, the stresses inside the system lie in the megapascal range, nearly three orders of magnitude smaller as compared to zero displacement boundary condition. Stress impact on reaction kinetics gets reduced considerably.

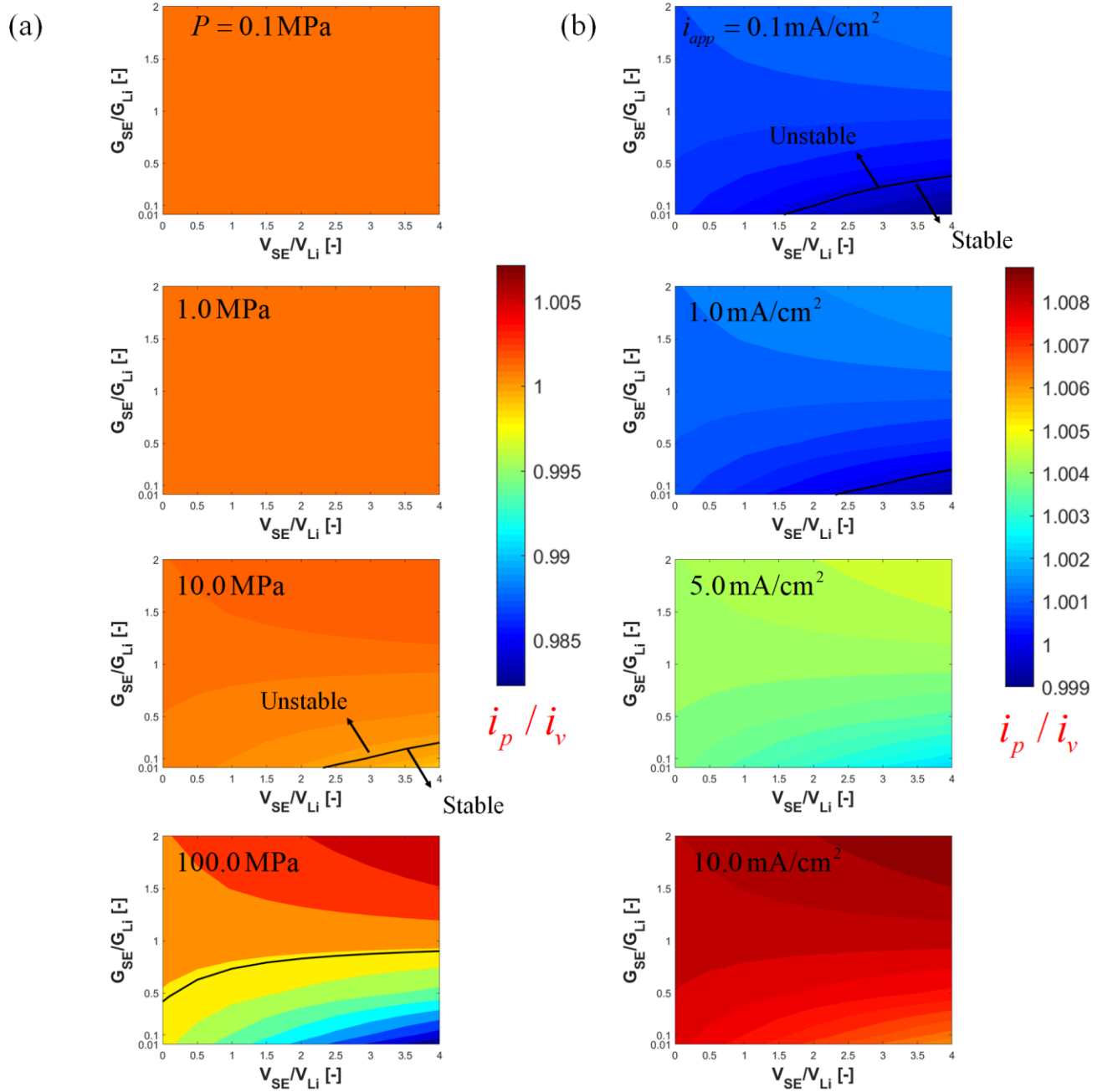


Fig. 5 (a) Impact of external pressure and (b) current density on deposition stability as a function of the shear modulus and molar volume ratio for electrochemical properties of inorganic LLZO electrolyte (@ 25°C: $i_0 = 5.5 \text{ A/m}^2$, $\kappa = 0.10 \text{ S/m}$). As external pressure is increased, deposition stability improves across all molar volume ranges only for very low shear modulus ratio. As current density is increased, transport and kinetic overpotentials increase, resulting in stable deposition only at low current densities.

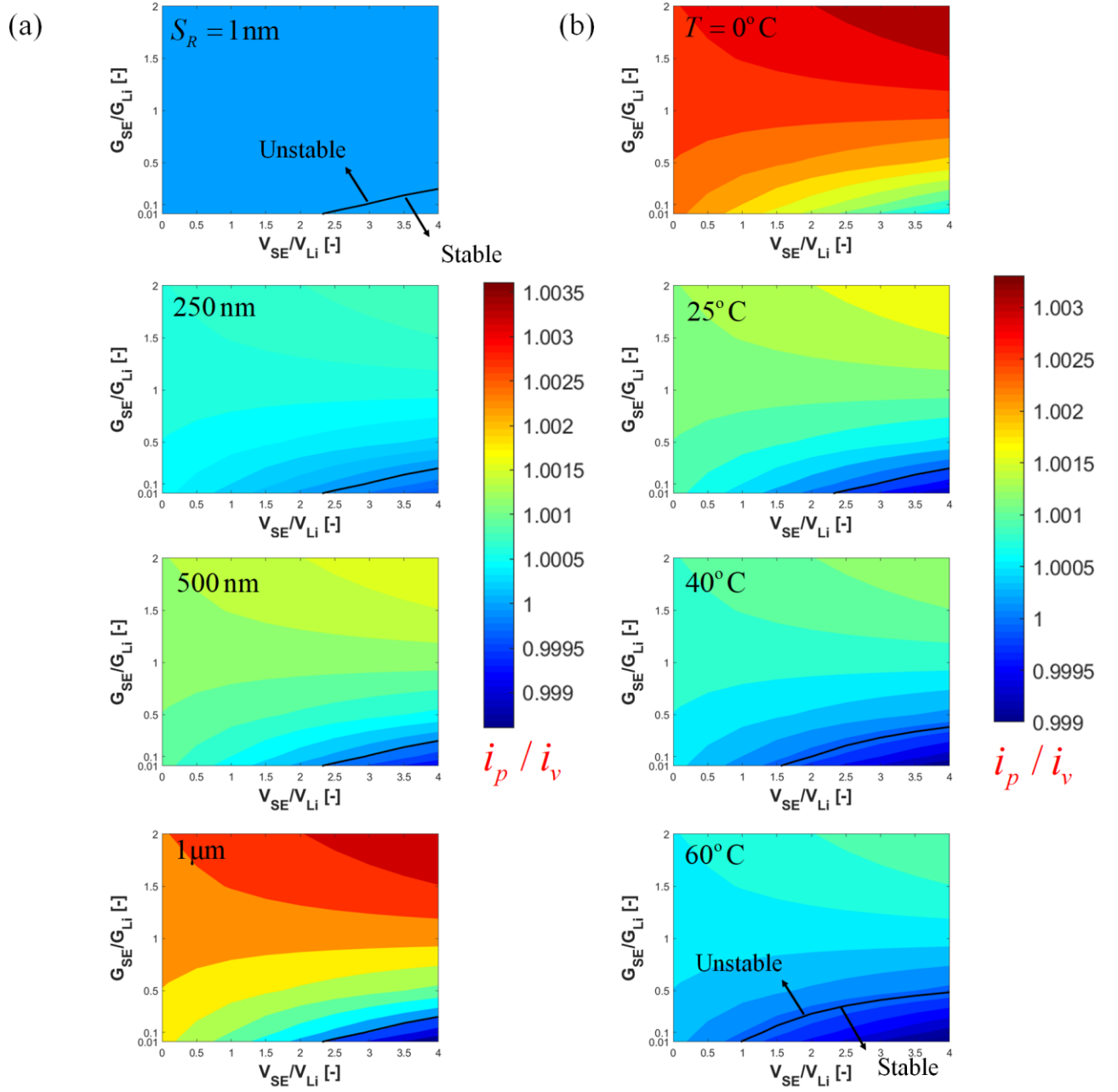


Fig. 6 (a) Impact of surface roughness and (b) temperature on deposition stability as a function of the shear modulus and molar volume ratio for electrochemical properties of inorganic LLZO electrolyte (@ 25°C : $i_0 = 5.5 \text{ A/m}^2$, $\kappa = 0.10 \text{ S/m}$). As surface roughness is increased, deposition instability magnitudes increase in the unstable zone. As temperature is decreased,

transport and kinetic overpotentials increase, resulting in stable deposition only at high temperatures.

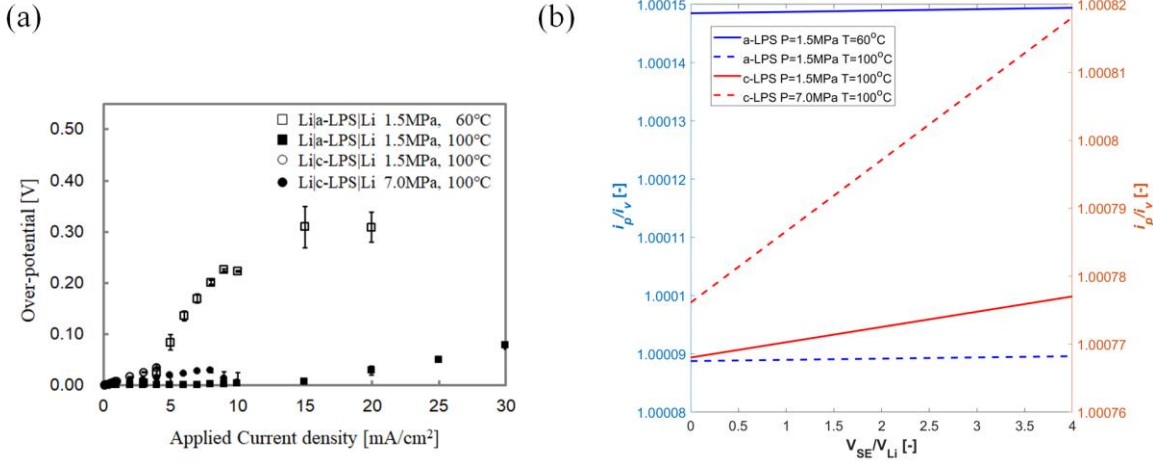


Fig. 7 Comparison between (a) experiments and (b) model for amorphous (a-LPS) and polycrystalline LPS (c-LPS) solid electrolyte. Amorphous LPS shows higher ionic conductivity ($0.4 > 0.3$ mS/cm) and smaller average surface roughness ($20.2 < 131.0$ nm) as compared to crystalline LPS. Amorphous LPS exhibits higher critical current densities and lower overpotentials as compared to crystalline LPS for same external pressure and temperature. As temperature increase, the deposition stability improves for all molar volume ratios investigated which can be correlated qualitatively with the overpotential decrease in symmetric cell experiments. An interesting result is that pressure increase results in more deposition instability from numerical computations for the LPS system investigated.

Supplementary Information

Microstructure and Pressure Driven Electrodeposition Stability in Solid-State Batteries

Ankit Verma¹, Hiroki Kawakami², Hiroyuki Wada², Anna Hirowatari², Nobuhisa Ikeda², Yoshifumi Mizuno², Toshikazu Kotaka², Koichiro Aotani², Yuichiro Tabuchi², and Partha P. Mukherjee^{1z}

¹School of Mechanical Engineering, Purdue University, West Lafayette, IN, USA

²Nissan Research Center, Nissan Motor Co., Ltd., Natsushima, Yokosuka, Kanagawa 237-8523, Japan

*Correspondence: pmukherjee@purdue.edu

Continuum Mechanics for Linear Elasticity (Small displacement, Strain and Stress)

The constitutive relations for stress-strain in an elastic medium are given as¹

$$\begin{aligned}\varepsilon_{xx} &= \frac{1}{E}(\sigma_{xx} - \nu(\sigma_{yy} + \sigma_{zz})) \\ \varepsilon_{yy} &= \frac{1}{E}(\sigma_{yy} - \nu(\sigma_{xx} + \sigma_{zz})) \\ \varepsilon_{zz} &= \frac{1}{E}(\sigma_{zz} - \nu(\sigma_{xx} + \sigma_{yy})) \\ \varepsilon_{xy} &= \frac{\sigma_{xy}}{2G}, \quad \varepsilon_{yz} = \frac{\sigma_{yz}}{2G}, \quad \varepsilon_{xz} = \frac{\sigma_{xz}}{2G}\end{aligned}\tag{1}$$

Here, ε_{ij} are the strain components and σ_{ij} are the stress components with $i=j$ corresponding to the normal strain/stress components and $i \neq j$ corresponding to the shear strain/stress components respectively. E is the Young's modulus, G is the shear modulus, and ν is the Poisson's ratio of the material medium of interest.

The stress-strain constitutive relations can also be written in indicial notation as

$$\begin{aligned}\varepsilon_{ij} &= \frac{1}{E}[(1+\nu)\sigma_{ij} - \nu\sigma_{kk}\delta_{ij}] \\ \sigma_{ij} &= 2GE_{ij} + \lambda\varepsilon_{kk}\delta_{ij} \\ G &= \frac{E}{2(1+\nu)}, \quad \lambda = \frac{2\nu G}{1-2\nu}\end{aligned}\tag{2}$$

Here, summation over the repeated indices is implied. ε_{ij} and σ_{ij} are the 2nd order strain and stress tensor respectively while δ_{ij} is the 2nd order Kronecker delta tensor.

Note that, the equations for stress and strain can be written interchangeably in terms of each other, i.e. strain as a function of stress, $\varepsilon_{ij} = f(\sigma_{ij})$, and stress as a function of strain, $\sigma_{ij} = f(\varepsilon_{ij})$. The shear modulus G and material coefficient λ are also referred to as Lamé parameters. The total stress tensor can be written as a sum of its deviatoric,

τ_{ij}^d , and hydrostatic stress , σ_{ij}^h ,components as

$$\begin{aligned}\sigma_{ij} &= \tau_{ij}^d + \sigma_{ij}^h \\ \sigma_{ij}^h &= \frac{1}{3} \delta_{ij} \sigma_{kk} \\ \tau_{ij}^d &= \sigma_{ij} - \frac{1}{3} \delta_{ij} \sigma_{kk}\end{aligned}\tag{3}$$

Finally, the linear elasticity strain-displacement correlation is given as

$$\varepsilon_{ij} = \frac{1}{2} \left(\frac{\partial u_i}{\partial x_j} + \frac{\partial u_j}{\partial x_i} \right)\tag{4}$$

Here, u_i corresponds to the displacement in the i -th direction. In the general 3D case, the displacement vector, \vec{u} , has three components u,v,w corresponding to the displacements in the x, y and z directions respectively.

The quasistatic stress balance in the absence of body forces takes the form (in vector and index notations)

$$\nabla \cdot \vec{\sigma} = 0 \Rightarrow \frac{\partial \sigma_{ij}}{\partial x_i} = 0, \quad (j = 1, 2, 3)\tag{5}$$

Substitution of the stress-strain constitutive relations (Eq. (2)) followed by the strain-displacement (Eq. (3)) equations into the quasistatic force balance leads us to the displacement equations in Eq. (5) given in index notation.

$$\begin{aligned}G \nabla^2 u_i + (\lambda + G) \frac{\partial^2 u_k}{\partial x_k \partial x_i} &= 0 \\ \Rightarrow \nabla^2 u_i + \frac{1}{1-2\nu} \frac{\partial^2 u_k}{\partial x_k \partial x_i} &= 0\end{aligned}\tag{6}$$

For our two-dimensional domain, the corresponding x and y displacement equations for u, v take the form

$$\begin{aligned}\frac{\partial^2 u}{\partial x^2} + \frac{\partial^2 u}{\partial y^2} + \frac{1}{(1-2\nu)} \left[\frac{\partial^2 u}{\partial x^2} + \frac{\partial^2 v}{\partial x \partial y} \right] &= 0 \\ \frac{\partial^2 v}{\partial x^2} + \frac{\partial^2 v}{\partial y^2} + \frac{1}{(1-2\nu)} \left[\frac{\partial^2 u}{\partial x \partial y} + \frac{\partial^2 v}{\partial y^2} \right] &= 0\end{aligned}\tag{7}$$

Monroe-Newman Configuration: Zero Displacement Boundary Condition at the Far Field

The solutions to the displacement equations for far-field displacement tending to zero have been elucidated in the seminal work of Monroe-Newman² for the two-dimensional Li metal-solid electrolyte domain extending to infinity in the y -direction (semi-infinite domain). Herein, electrode surface lies at $y=0$ with electrode and electrolyte extending infinitely away from this interface. The corresponding far-field displacement boundary conditions take the form

$$\begin{aligned}u(x, y \rightarrow \pm\infty) &= 0 \\ v(x, y \rightarrow \pm\infty) &= 0\end{aligned}\tag{8}$$

while the sinusoidal interfacial displacement is prescribed at the metal-solid electrolyte interface as

$$v(x, 0) = A \cos(kx)\tag{9}$$

Furthermore, balance of surface forces at the metal-electrolyte interface at $y=0$ is given by

$$\vec{t}(x, 0) \cdot \left\{ \vec{n}(x, 0) \cdot \left[\vec{\tau}_{Li}^d(x, 0) - \vec{\tau}_{SE}^d(x, 0) \right] \right\} = 0\tag{10}$$

Here, $\vec{t}(x, 0)$ is the tangent vector at the interface, $\vec{n}(x, 0)$ is the normal vector at the interface and $\vec{\tau}_{Li}^d(x, 0)$, $\vec{\tau}_{SE}^d(x, 0)$ are the interfacial ($y=0$) deviatoric stresses in the Li metal and solid electrolyte domain respectively.

For the sake of completeness and the calculation of stress contours for the zero-

displacement condition, we report the solution procedure and the final stress solutions herein. The general displacement solution can be obtained by assuming its functional form to be variable separable i.e. a product of two functions each depending only on one spatial coordinate, x or y .

$$\vec{u} = \begin{bmatrix} u \\ v \end{bmatrix} = \operatorname{Re} \left\{ e^{ikx} \begin{bmatrix} X(y) \\ Y(y) \end{bmatrix} \right\}; \quad u = e^{ikx} X, \quad v = e^{ikx} Y \quad (11)$$

The solution procedure requires the insertion of the general displacement solution (Eq. (11)) into the partial differential equation for displacement (Eq. (7)) necessitating the computation of the corresponding spatial partial derivatives (individual terms of Eq. (7)).

$$\begin{aligned} \frac{\partial^2 u}{\partial x^2} &= (ik)^2 X e^{ikx} = -k^2 X e^{ikx}; \quad \frac{\partial^2 u}{\partial y^2} = \frac{d^2 X}{dy^2} e^{ikx}; \quad \frac{\partial^2 v}{\partial x \partial y} = ik \frac{d Y}{dy} e^{ikx} \\ \frac{\partial^2 v}{\partial x^2} &= (ik)^2 Y e^{ikx} = -k^2 Y e^{ikx}; \quad \frac{\partial^2 v}{\partial y^2} = \frac{d^2 Y}{dy^2} e^{ikx}; \quad \frac{\partial^2 u}{\partial y \partial x} = ik \frac{d X}{dy} e^{ikx} \end{aligned} \quad (12)$$

It is interesting to note that the partial derivatives of u, v in x, y are now reduced to substantial derivatives of X, Y in y allowing for the conversion of the displacement partial differential equations to second order ordinary differential equations in y .

$$\begin{aligned} x\text{-direction: } &-k^2 X e^{ikx} + \frac{d^2 X}{dy^2} e^{ikx} + \frac{1}{1-2\nu} \left[-k^2 X e^{ikx} + (ik) \frac{d Y}{dy} e^{ikx} \right] = 0 \\ \Rightarrow &-k^2 X + \frac{d^2 X}{dy^2} + \frac{1}{1-2\nu} \left[-k^2 X + (ik) \frac{d Y}{dy} \right] = 0 \end{aligned} \quad (13)$$

$$\begin{aligned} y\text{-direction: } &-k^2 Y e^{ikx} + \frac{d^2 Y}{dy^2} e^{ikx} + \frac{1}{1-2\nu} \left[ik \frac{d X}{dy} e^{ikx} + \frac{d^2 Y}{dy^2} e^{ikx} \right] = 0 \\ \Rightarrow &-k^2 Y + \frac{d^2 Y}{dy^2} + \frac{1}{1-2\nu} \left[ik \frac{d X}{dy} + \frac{d^2 Y}{dy^2} \right] = 0 \end{aligned} \quad (14)$$

Here, e^{ikx} is common and can be cancelled out from the left-hand side of the equation.

The above 2nd order ordinary differential equations are now amenable to solution through Laplace transform with respect to y . Taking the Laplace transform of Eqs. (13, 14), we get

$$\begin{aligned} x\text{-direction : } & -k^2 \bar{X} + [s^2 \bar{X} - s \bar{X}(0) - \bar{X}'(0)] + \frac{1}{1-2\nu} [-k^2 \bar{X} + ik(s \bar{Y} - \bar{Y}(0))] = 0 \\ y\text{-direction : } & -k^2 \bar{Y} + [s^2 \bar{Y} - s \bar{Y}(0) - \bar{Y}'(0)] + \frac{1}{1-2\nu} \{ik(s \bar{X} - \bar{X}(0)) + [s^2 \bar{Y} - s \bar{Y}(0) - \bar{Y}'(0)]\} = 0 \end{aligned} \quad (15)$$

Here, the barred variables indicate the transformed functions, s is the transformed y -coordinate, and the prime superscript indicates differentiation with respect to y .

Rearranging the terms, we get

$$\begin{aligned} x\text{-direction : } & 2(1-\nu)k^2 \bar{X} - (1-2\nu)[s^2 \bar{X} - s \bar{X}(0) - \bar{X}'(0)] - ik(s \bar{Y} - \bar{Y}(0)) = 0 \\ y\text{-direction : } & k^2(1-2\nu) \bar{Y} - 2(1-\nu)[s^2 \bar{Y} - s \bar{Y}(0) - \bar{Y}'(0)] - ik(s \bar{X} - \bar{X}(0)) = 0 \end{aligned} \quad (16)$$

Eq. (16) can be rewritten in matrix form as

$$\begin{bmatrix} (1-2\nu)s^2 - 2(1-\nu)k^2 & iks \\ iks & 2(1-\nu)s^2 - (1-2\nu)k^2 \end{bmatrix} \begin{bmatrix} X \\ Y \end{bmatrix} = \begin{bmatrix} (1-2\nu)[s \bar{X}(0) + \bar{X}'(0)] + ik \bar{Y}(0) \\ 2(1-\nu)[s \bar{Y}(0) + \bar{Y}'(0)] + ik \bar{X}(0) \end{bmatrix} \quad (17)$$

Here, the coefficient square matrix, A , and the RHS vector, C , can be delineated as shown below

$$A = \begin{bmatrix} a_1 & b_1 \\ a_2 & b_2 \end{bmatrix} = \begin{bmatrix} (1-2\nu)s^2 - 2(1-\nu)k^2 & iks \\ iks & 2(1-\nu)s^2 - (1-2\nu)k^2 \end{bmatrix} \quad (18)$$

$$C = \begin{bmatrix} c_1 \\ c_2 \end{bmatrix} = \begin{bmatrix} (1-2\nu)[s \bar{X}(0) + \bar{X}'(0)] + ik \bar{Y}(0) \\ 2(1-\nu)[s \bar{Y}(0) + \bar{Y}'(0)] + ik \bar{X}(0) \end{bmatrix} \quad (19)$$

The determinant is evaluated

$$\det(A) = a_1 b_2 - b_1 a_2 = 2(1-\nu)(1-2\nu)(s^2 - k^2)^2 \quad (20)$$

Using Cramer's rule, we find out the solution of the transformed functions

$$\begin{aligned} \bar{X} &= \frac{c_1 b_2 - b_1 c_2}{\det(A)} = \frac{f(s^3)}{f(s^4)} \\ \bar{Y} &= \frac{a_1 c_2 - c_1 a_2}{\det(A)} = \frac{f(s^3)}{f(s^4)} \end{aligned} \quad (21)$$

The above exercise allows us to use the theorem of residues to obtain the inverted solution of the form

$$\begin{bmatrix} X(y) \\ Y(y) \end{bmatrix} = \begin{bmatrix} c_1 e^{-ky} + c_2 y e^{-ky} + c_3 e^{ky} + c_4 y e^{ky} \\ c_5 e^{-ky} + c_6 y e^{-ky} + c_7 e^{ky} + c_8 y e^{ky} \end{bmatrix} \quad (22)$$

Computation of the constants requires implementation of the boundary conditions. We demonstrate the solution for the solid electrolyte domain ($y > 0$), the solution for the Li metal domain ($y < 0$) can be computed analogously. For the solid electrolyte ($y > 0$), the e^{ky} terms diverge as $y \rightarrow \infty$, consequently the corresponding constants c_3, c_4, c_7, c_8 should be zero to obtain a bounded displacement function. The displacement functions now take the form

$$\begin{bmatrix} u(x, y) \\ v(x, y) \end{bmatrix} = \operatorname{Re} \left\{ e^{ikx} \begin{bmatrix} c_1 e^{-ky} + c_2 y e^{-ky} \\ c_5 e^{-ky} + c_6 y e^{-ky} \end{bmatrix} \right\} \quad (23)$$

Furthermore, the sinusoidal nature of the perturbation function given by Eq. (9), $v(x, 0) = A \cos(kx)$ necessitates that the coefficients c_5, c_6 be real while the coefficients c_1, c_2 can contain both real and imaginary components, i.e.,

$$\begin{aligned} c_1 &= f_1 - ig_1 \\ c_2 &= f_2 - ig_2 \end{aligned} \quad (24)$$

Subsequent insertion into Eq. (23) reveals the following form to us

$$\begin{bmatrix} u(x, y) \\ v(x, y) \end{bmatrix} = \operatorname{Re} \left\{ e^{ikx} \begin{bmatrix} (f_1 - ig_1)e^{-ky} + (f_2 - ig_2)c_2 ye^{-ky} \\ c_5 e^{-ky} + c_6 ye^{-ky} \end{bmatrix} \right\} \quad (25)$$

The real part of Eq. (25) gives

$$\begin{bmatrix} u(x, y) \\ v(x, y) \end{bmatrix} = \cos(kx)e^{-ky} \begin{bmatrix} f_1 + f_2 y \\ c_5 + c_6 y \end{bmatrix} + \sin(kx)e^{-ky} \begin{bmatrix} g_1 + g_2 y \\ 0 \end{bmatrix} \quad (26)$$

We now get the form of the displacement solutions requiring a determination of the constants $f_1, f_2, g_1, g_2, c_5, c_6$. Substitution of the displacement solutions given by Eq. (26) into the original governing partial differential equation for displacement given by Eq. (7) and utilization of the linear independence property of sine and cosine functions allows us to get a value for these constants. This procedure is detailed in Eqs. (27-36).

$$\begin{aligned} &[f_1 k + 2(1-2\nu)f_2 + f_2 ky] \cos(kx) \\ &+ \{(c_5 - g_1)k - [2(1-2\nu)g_2 + c_6] + (c_6 - g_2)ky\} \sin(kx) = 0 \end{aligned} \quad (27)$$

$$\begin{aligned} &\{(c_5 - g_1)k + [g_2 - 4(1-\nu)c_6] + (c_6 - g_2)ky\} \cos(kx) \\ &+ (f_1 k - f_2 + f_2 ky) \sin(kx) = 0 \end{aligned} \quad (28)$$

Using linear independence of sine and cosine we get

$$f_1 k + 2(1-2\nu)f_2 + f_2 ky = 0 \quad (29)$$

$$(c_5 - g_1)k - [2(1-2\nu)g_2 + c_6] + (c_6 - g_2)ky = 0 \quad (30)$$

$$(c_5 - g_1)k + [g_2 - 4(1-\nu)c_6] + (c_6 - g_2)ky = 0 \quad (31)$$

$$f_1 k - f_2 + f_2 ky = 0 \quad (32)$$

Furthermore, the constant and spatial coordinate y -dependent terms should independently sum to zero for the above equalities to hold. Thus, we get eight equations in six unknowns, with two redundant equations

$$\begin{aligned} f_1 k + 2(1-2\nu) f_2 &= 0 \\ f_2 k &= 0 \end{aligned} \quad (33)$$

$$\begin{aligned} (c_5 - g_1)k - [2(1-2\nu)g_2 + c_6] &= 0 \\ (c_6 - g_2)k &= 0 \end{aligned} \quad (34)$$

$$\begin{aligned} (c_5 - g_1)k + [g_2 - 4(1-\nu)c_6] &= 0 \\ (c_6 - g_2)k &= 0 \end{aligned} \quad (35)$$

$$\begin{aligned} f_1 k - f_2 &= 0 \\ f_2 k &= 0 \end{aligned} \quad (36)$$

Consequently, the constants and the solid electrolyte displacement solution take the form

$$\begin{aligned} f_1 &= 0 \\ f_2 &= 0 \\ g_2 &= c_6 \\ g_1 &= c_5 - \frac{3-4\nu}{k} c_6 \end{aligned} \quad (37)$$

$$\begin{bmatrix} u(x, y \geq 0) \\ v(x, y \geq 0) \end{bmatrix} = \begin{bmatrix} \left(c_5 - \frac{3-4\nu}{k} c_6 + c_6 y \right) \sin(kx) \\ (c_5 + c_6 y) \cos(kx) \end{bmatrix} e^{-ky} \quad (38)$$

For the Li metal domain ($y < 0$), a similar procedure can be used to delineate the displacement solution

$$\begin{bmatrix} u(x, y \leq 0) \\ v(x, y \leq 0) \end{bmatrix} = \begin{bmatrix} -\left(c_7 + \frac{3-4\nu}{k} c_8 + c_8 y \right) \sin(kx) \\ (c_7 + c_8 y) \cos(kx) \end{bmatrix} e^{ky} \quad (39)$$

Matching the interfacial perturbation at $y = 0$, we get

$$c_5 = c_7 = A \quad (40)$$

and the displacements in the solid electrolyte and Li metal domain as

$$\begin{bmatrix} u \\ v \end{bmatrix}_{SE} = \begin{bmatrix} \left(A - \frac{3-4\nu_{SE}}{k} B + By \right) \sin(kx) e^{-ky} \\ (A + By) \cos(kx) e^{-ky} \end{bmatrix} \quad (41)$$

$$\begin{bmatrix} u \\ v \end{bmatrix}_{Li} = \begin{bmatrix} \left(A - \frac{3-4\nu_{SE}}{k} B + \left(\frac{2k}{3-4\nu_{Li}} A - \frac{3-4\nu_{SE}}{3-4\nu_{Li}} B \right) y \right) \sin(kx) e^{ky} \\ \left(A - \left(\frac{2k}{3-4\nu_{Li}} A - \frac{3-4\nu_{SE}}{3-4\nu_{Li}} B \right) y \right) \cos(kx) e^{ky} \end{bmatrix} \quad (42)$$

It should be noted here that in Monroe *et al.*, the corresponding displacement equation for Li metal domain has a slight error in the solution for y -direction displacement; the coefficient A has been written as B in the term corresponding to $\frac{2k}{3-4\nu_{Li}} A$. Finally, the constants A and B can be correlated through the balance of the surface force at the interface given by Eq. (10) with the correlation given below

$$B = A \frac{k [G_{SE} (3-4\nu_{Li}) + G_{Li}]}{2 [G_{SE} (3-4\nu_{Li}) (1-\nu_{SE}) + G_{Li} (3-4\nu_{SE}) (1-\nu_{Li})]} \quad (43)$$

The stresses can now be computed from the displacement conditions using Eq. (2).

Constant External Pressure Boundary Condition: Constant Compressive Stress at the Far Field

Here, the Airy Stress formalism can be used to compute the stresses throughout the Li metal-solid electrolyte domain in accordance with Angheluta *et al.*³ The stress boundary conditions for a normal load applied in the y -direction at far field corresponds to

$$\begin{aligned}\sigma_{yy}(x, y \rightarrow \pm\infty) &= -|P_{ext}| \\ \sigma_{xy}(x, y \rightarrow \pm\infty) &= 0\end{aligned}\quad (44)$$

Continuity of stress vector across the interface follows from force balance and additionally we require that $u(x \rightarrow \pm\infty, y) = 0$. For the perfectly flat interface, this gives the Airy function of the form

$$\begin{aligned}\varphi_{SE}^{flat}(x, y) &= -\frac{P_{ext}}{2}(x^2 + v_{SE}y^2) \\ \varphi_{Li}^{flat}(x, y) &= -\frac{P_{ext}}{2}(x^2 + v_{Li}y^2)\end{aligned}\quad (45)$$

For the perturbed interface, superposition principle of the Airy stress function is utilized to combine the solution to the flat interface and correction due to the undulation as follows

$$\begin{aligned}\varphi_{SE}(x, y) &= \varphi_{SE}^{flat}(x, y) + \varphi_{SE}^{pert}(x, y) \\ \varphi_{Li}(x, y) &= \varphi_{Li}^{flat}(x, y) + \varphi_{Li}^{pert}(x, y)\end{aligned}\quad (46)$$

The Airy stress function for the perturbation takes the form

$$\begin{aligned}\varphi_{SE}^{pert}(x, y) &= \frac{-|P_{ext}| A \cos(kx) \exp(-ky)(\alpha_{SE}y + \beta)}{k(G_{Li}\tilde{\kappa}_{SE} + G_{SE})(G_{SE}\tilde{\kappa}_{Li} + G_{Li})} \\ \varphi_{Li}^{pert}(x, y) &= \frac{|P_{ext}| A \cos(kx) \exp(ky)(\alpha_{Li}y - \beta)}{k(G_{Li}\tilde{\kappa}_{SE} + G_{SE})(G_{SE}\tilde{\kappa}_{Li} + G_{Li})}\end{aligned}\quad (47)$$

with material specific constants given by $\tilde{\kappa}_{SE}$, $\tilde{\kappa}_{Li}$, α_{SE} , α_{Li} and β . The relations for the constants under plane strain configuration are given in Eq. (48). For plane stress, only the parameters $\tilde{\kappa}_{SE}$, $\tilde{\kappa}_{Li}$ get varied. An interesting observation is the exponential decay of the perturbation effect in the form of $\exp(|ky|)$ at positions away from the interface

$$\begin{aligned}
\tilde{\kappa}_{SE} &= 3 - 4\nu_{SE}, \quad \tilde{\kappa}_{Li} = 3 - 4\nu_{Li} \\
\alpha_{SE} &= k(1 - \nu_{SE})(G_{Li} - G_{SE})(G_{SE}\tilde{\kappa}_{Li} + G_{Li}) \\
\alpha_{Li} &= k(1 - \nu_{Li})(G_{SE} - G_{Li})(G_{Li}\tilde{\kappa}_{SE} + G_{SE}) \\
\beta &= 2G_{SE}^2 \frac{1 - \nu_{Li}}{1 + \nu_{Li}} - 2G_{Li}^2 \frac{1 - \nu_{SE}}{1 + \nu_{SE}} + 4G_{SE}G_{Li} \frac{\nu_{SE} - \nu_{Li}}{(1 + \nu_{Li})(1 + \nu_{SE})}
\end{aligned} \tag{48}$$

The computation of the stresses can then be performed using the Airy stress functions from the relations

$$\sigma_{xx} = \frac{\partial^2 \varphi}{\partial y^2}, \quad \sigma_{yy} = \frac{\partial^2 \varphi}{\partial x^2}, \quad \sigma_{xy} = -\frac{\partial^2 \varphi}{\partial x \partial y} \tag{49}$$

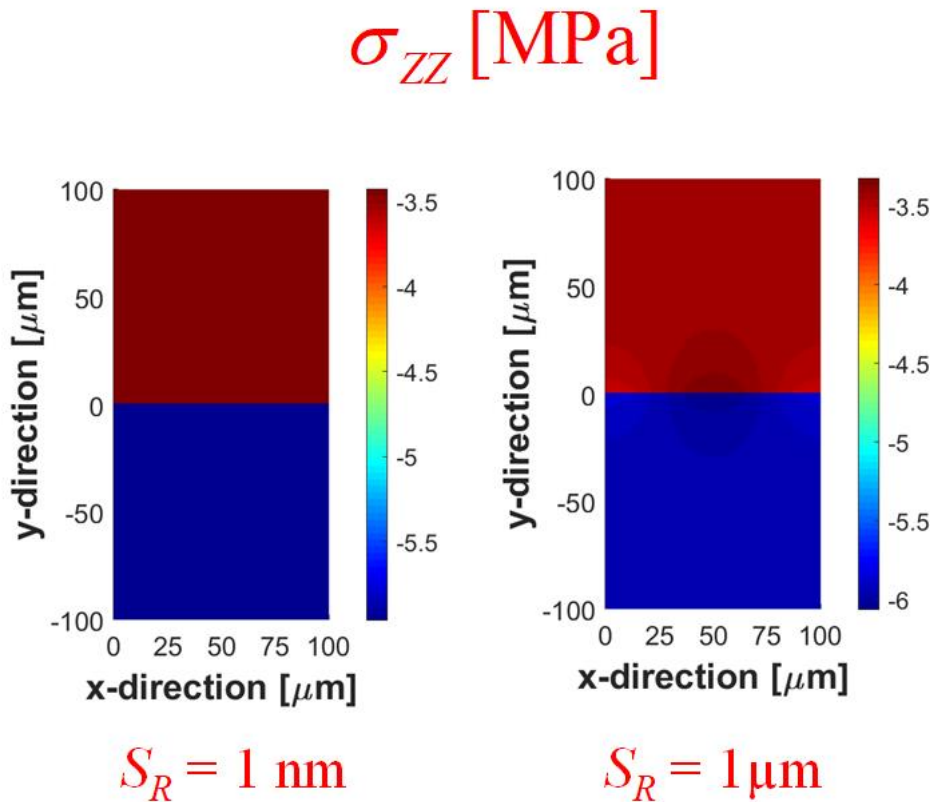


Fig. S1 Stress contours for σ_{zz} in the Li metal (bottom) – solid electrolyte (top) domain for constant external pressure of 10 MPa and interfacial perturbation amplitude.

Impact of Operating Conditions

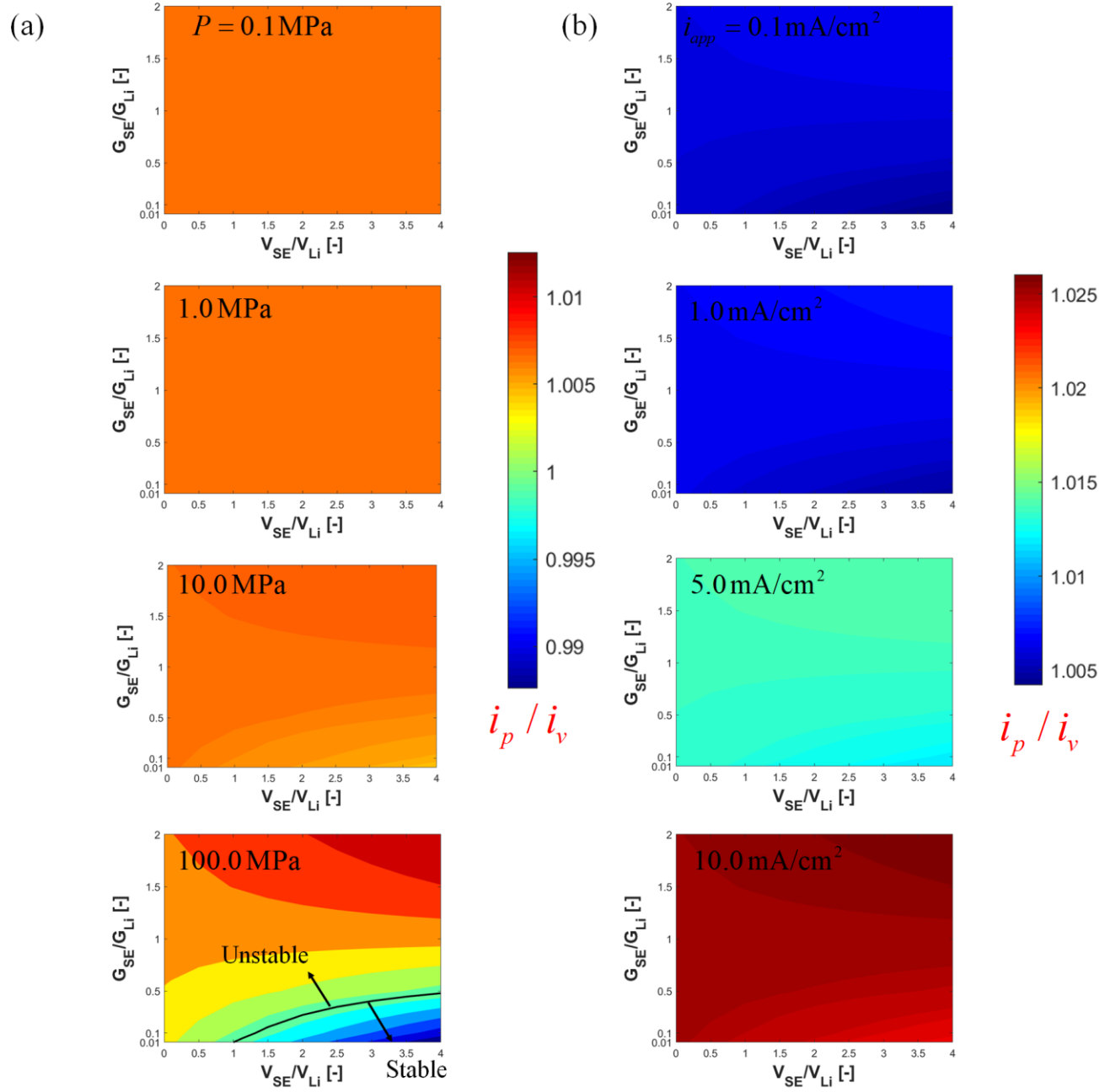


Fig. S2 (a) Impact of external pressure and (b) current density on deposition stability as a function of the shear modulus and molar volume ratio for electrochemical properties of amorphous sulfide electrolyte (@ 25°C : $i_0 = 12.6 \text{ A/m}^2$, $\kappa = 0.04 \text{ S/m}$).

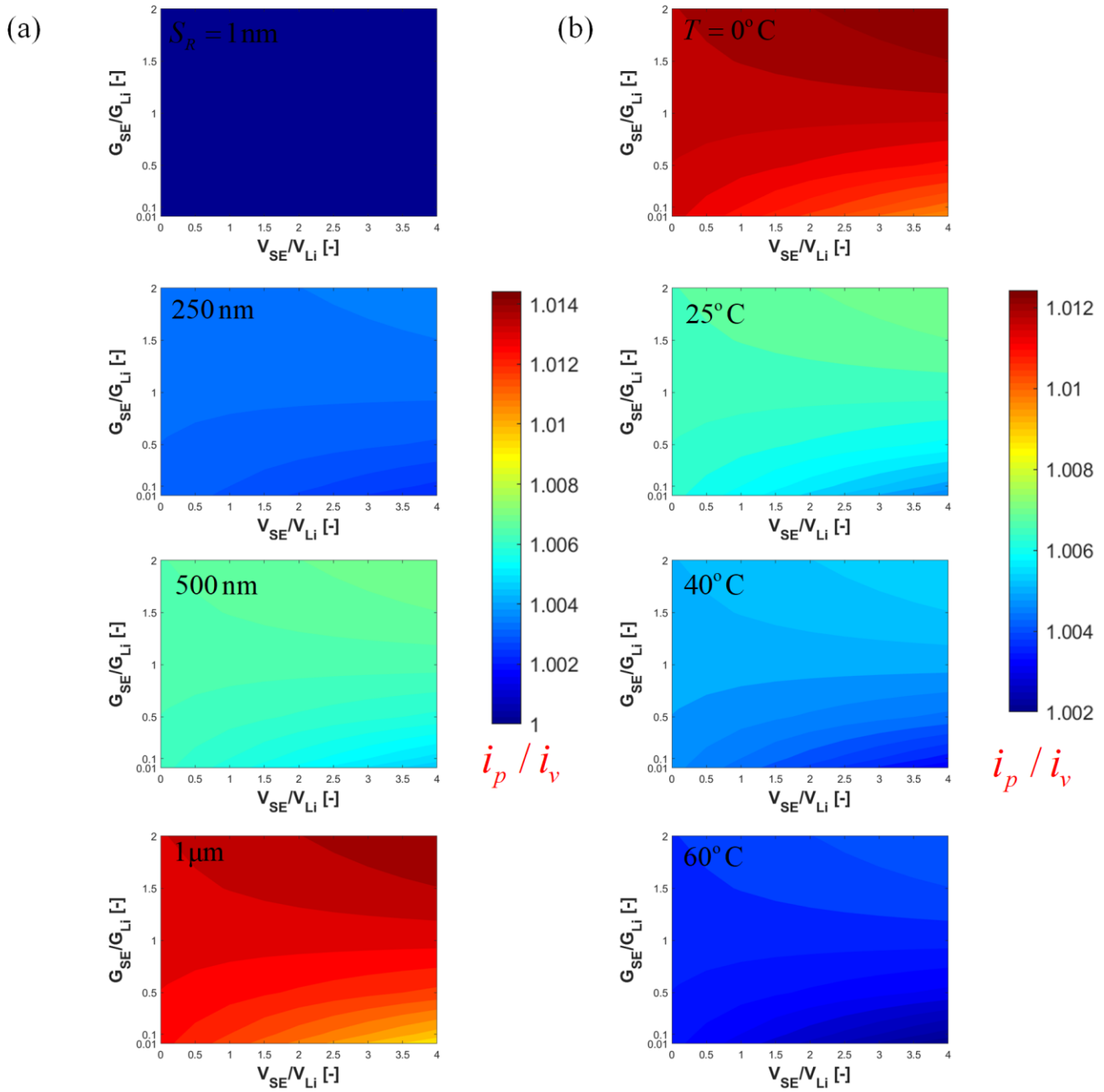


Fig. S3 (a) Impact of surface roughness and (b) temperature on deposition stability as a function of the shear modulus and molar volume ratio for electrochemical properties of amorphous sulfide electrolyte (@ 25°C : $i_0 = 12.6 \text{ A/m}^2$, $\kappa = 0.04 \text{ S/m}$).

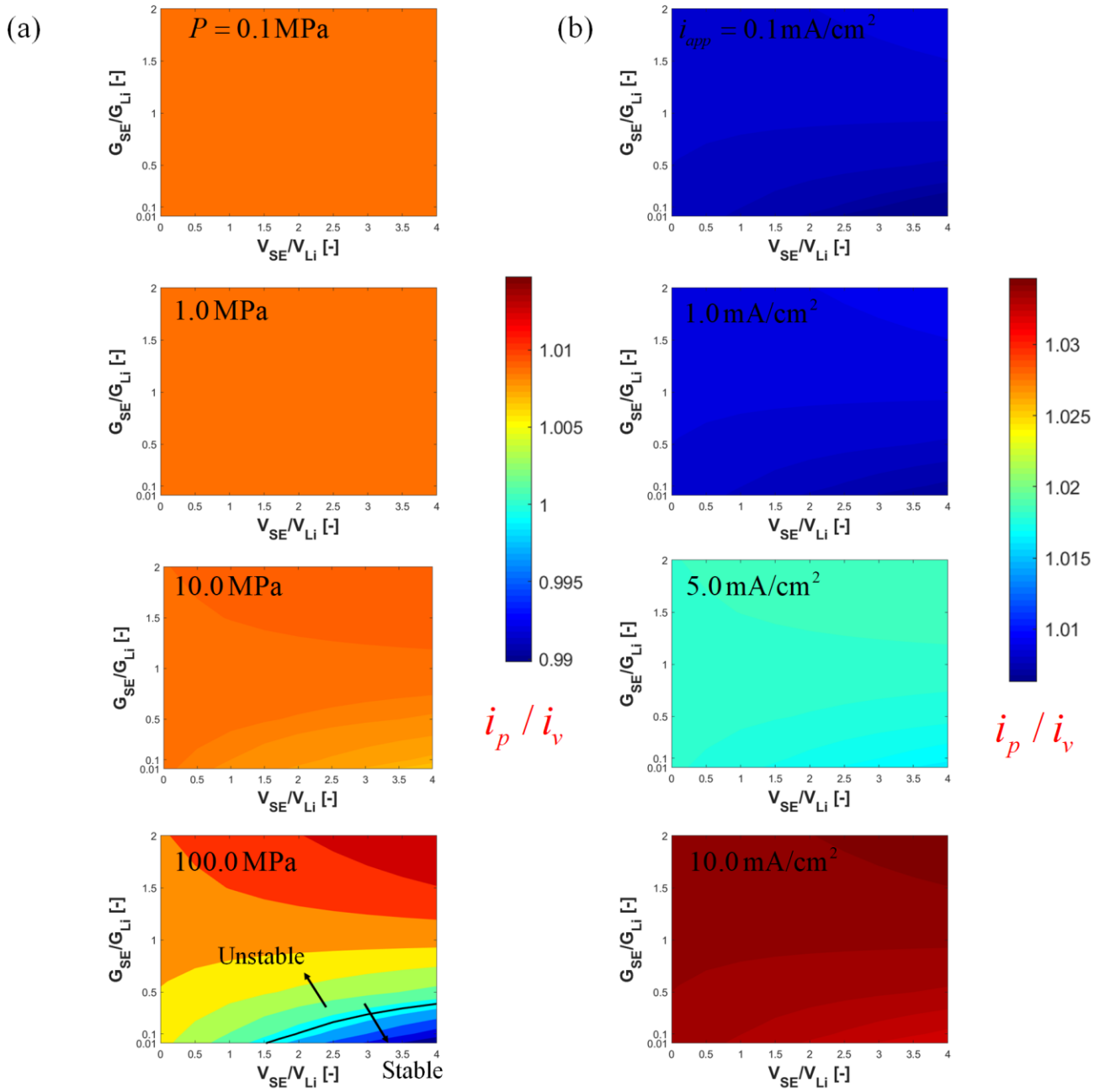


Fig. S4 (a) Impact of external pressure and (b) current density on deposition stability as a function of the shear modulus and molar volume ratio for electrochemical properties of crystalline sulfide electrolyte (@ 25°C: $i_0 = 12.6 \text{ A/m}^2$, $\kappa = 0.03 \text{ S/m}$).

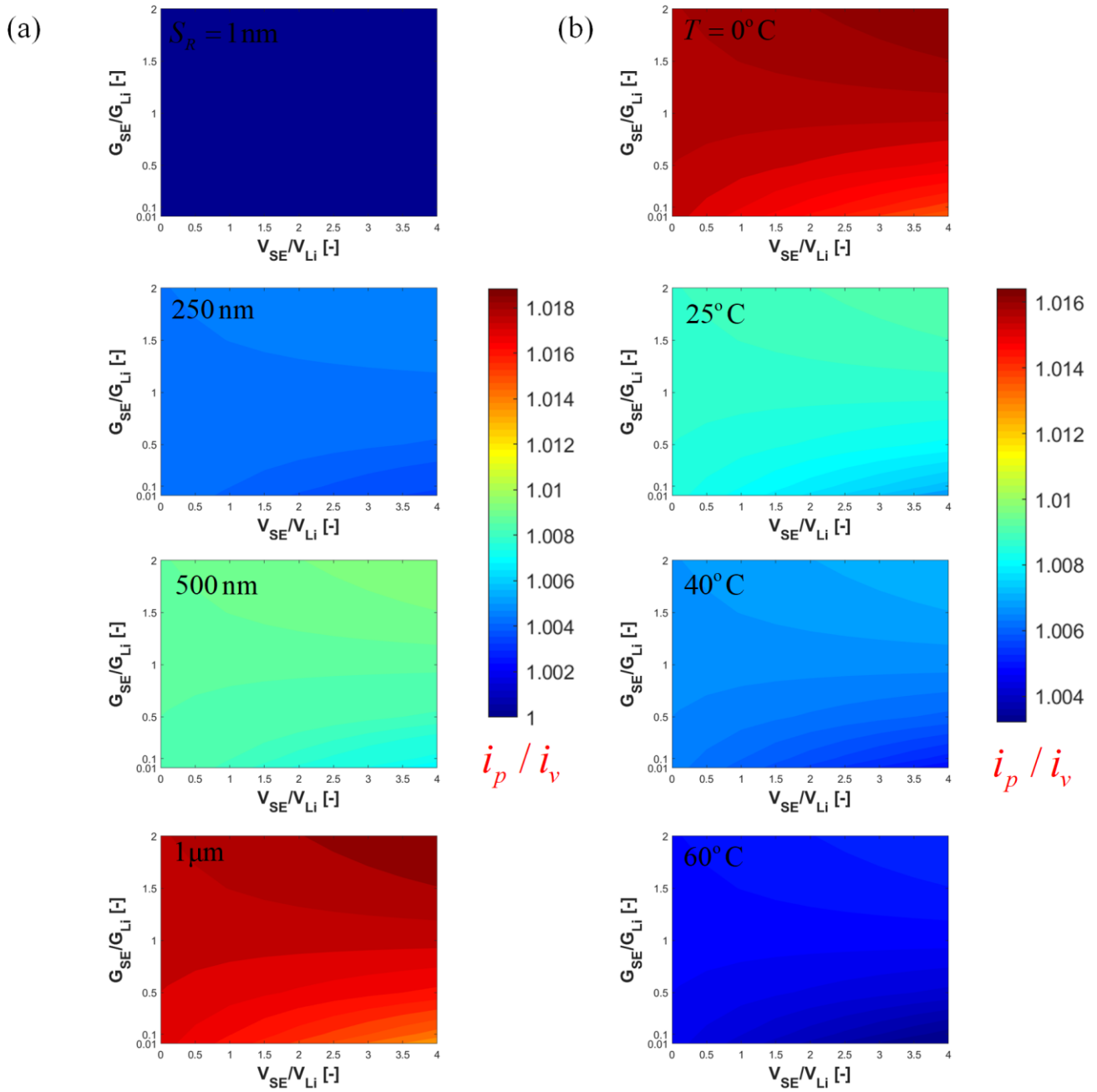


Fig. S5 (a) Impact of surface roughness and (b) temperature on deposition stability as a function of the shear modulus and molar volume ratio for electrochemical properties of crystalline sulfide electrolyte (@ 25°C : $i_0 = 12.6 \text{ A/m}^2$, $\kappa = 0.03 \text{ S/m}$).

References

- (1) Zhang, X.; Shyy, W.; Sastry, A. M. Numerical simulation of intercalation-induced stress in Li-ion battery electrode particles. *Journal of the Electrochemical Society* **2007**, *154* (10), A910-A916.

- (2) Monroe, C.; Newman, J. The impact of elastic deformation on deposition kinetics at lithium/polymer interfaces. *Journal of The Electrochemical Society* **2005**, *152* (2), A396-A404.
- (3) Angheluta, L.; Jettestuen, E.; Mathiesen, J. Thermodynamics and roughening of solid-solid interfaces. *Physical Review E* **2009**, *79* (3), 031601.